



CHALMERS
UNIVERSITY OF TECHNOLOGY

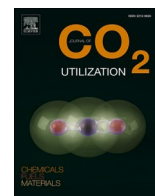
CO₂ hydrogenation to light olefins using In₂O₃ and SSZ-13 catalyst-Understanding the role of zeolite acidity in olefin production

Downloaded from: <https://research.chalmers.se>, 2024-03-20 09:37 UTC

Citation for the original published paper (version of record):

Di, W., Ho, H., Achour, A. et al (2023). CO₂ hydrogenation to light olefins using In₂O₃ and SSZ-13 catalyst-Understanding the role of zeolite acidity in olefin production. Journal of CO₂ Utilization, 72.
<http://dx.doi.org/10.1016/j.jcou.2023.102512>

N.B. When citing this work, cite the original published paper.



CO₂ hydrogenation to light olefins using In₂O₃ and SSZ-13 catalyst – Understanding the role of zeolite acidity in olefin production

Wei Di^a, Phuoc Hoang Ho^a, Abdenour Achour^a, Oleg Pajalic^b, Lars Josefsson^c, Louise Olsson^a, Derek Creaser^{a,*}

^a Chemical Engineering and Competence Centre for Catalysis, Chalmers University of Technology, Gothenburg, Sweden

^b Perstorp Specialty Chemicals AB, Perstorp, Sweden

^c Josefsson Sustainable Chemistry AB, Stenungsund, Sweden

ARTICLE INFO

Keywords:

CO₂ hydrogenation
Light olefins
SSZ-13
Al distribution
In₂O₃

ABSTRACT

With the aim to explore the effect of acidic properties of zeolites in tandem catalysts on their performance for CO₂ hydrogenation, two types of SSZ-13 zeolites with similar bulk composition, but different arrangements of framework Al, were prepared. Their morphology, pore structure, distribution of framework Al, surface acid strength and density, were explored. The results showed that SSZ-13 zeolites with isolated aluminum distribution could be successfully synthesized, however, they contained structural defects. During calcination, the framework underwent dealumination, resulting in weaker Brønsted acidity and lower crystallinity. The morphologies were, however, well preserved. Compared with the SSZ-13 zeolites, synthesized conventionally, these low acidity SSZ-13 zeolites with isolated aluminum were good zeolite components in bifunctional catalysts for CO₂ hydrogenation to light olefins. By combining with In₂O₃, they exhibited better catalytic performance for light olefin production during CO₂ hydrogenation at low temperatures. Na⁺ cation exchange was used to adjust the Brønsted acid site (BAS) density with only minor changes to the cavity structure. Comparative experiments established that the BAS density of the zeolite, rather than the framework Al distribution (BAS distribution), overwhelmingly affected catalyst stability and product selectivity. A higher acid density reduced the selectivity for light olefins, while lower acid density tended to form inert coke species leading to rapid deactivation. The ideal amount of BAS density in the bifunctional catalyst was approximately 0.25 mmol/g, which exhibited 70% selectivity for light olefins among hydrocarbons, and 74% selectivity for CO without deactivation, after 12 h reaction at 325 °C and 10 bar.

1. Introduction

Effectively converting waste CO₂ into basic chemical feedstocks can lead to sustainable production of green chemicals in the future [1,2]. One promising method is the catalytic conversion of CO₂ into high-value olefins by the use of hydrogen produced from renewable energy resources [3]. Over an oxide-zeolite (OXZEO) catalyst with bifunctional active sites for CO₂ hydrogenation and C–C bond formation, CO₂ can be efficiently converted via intermediate methanol or kenten into a mixture of short-chain olefins [4–6]. Compared to Fisher-Tropsch (FT) synthesis, this process can achieve a high selectivity for light olefins (C₂–C₄) among the hydrocarbon products [3–7].

Currently, several kinds of metal oxide catalysts have been reported for the activation of CO₂ to form methanol or other oxygenates,

including In₂O₃ [8], In₂O₃–ZrO₂ [4,9], ZnZrO_x [5,10], ZnGa₂O₄ [6] and Cu–Zn–MO_x (M = Al, Zr, or Zr–Ti) [11,12]. With the aim to produce olefins, the reports of zeolite/zeotype components in the OXZEO catalysts are extensively concentrated on SAPO-34 molecular sieves [4–6, 12]: the commercial methanol to olefins (MTO) catalysts with CHA topology and medium acidity. The SAPO-34 catalyzes C–C bond coupling to convert methanol to light olefins inside its micro-porous cages (10 × 6.7 Å) [13]. Its suitable Brønsted acidity and accessible cage size (3.8 × 3.8 Å) enables a low coke deposition rate and a high selectivity for light olefins during CO₂ or CO hydrogenation process by a delicate reaction path, involving a dynamic balance between two types of reactions: the MTO reaction and hydrogenation reactions [14]. Specifically, after methanol dehydration over the Brønsted acid sites, a large number of hydrocarbon pool (HCP) species (olefins, methylbenzenes) are formed

* Corresponding author.

E-mail address: derek.creaser@chalmers.se (D. Creaser).

<https://doi.org/10.1016/j.jcou.2023.102512>

Received 19 March 2023; Received in revised form 17 May 2023; Accepted 31 May 2023

Available online 6 June 2023

2212-9820/© 2023 The Author(s). Published by Elsevier Ltd. This is an open access article under the CC BY license (<http://creativecommons.org/licenses/by/4.0/>).

and trapped in the cage, and serve as organic co-catalytic centers for light olefin formation, as well as for coke accumulation leading to deactivation [13]. At the same time, due to co-feeding of H₂ throughout the process, the hydrogenation of coke precursors, including formaldehyde and 1,3-butadiene, occurs over the Brønsted acid sites (BAS) of the catalyst. The hydrogenation reactions alleviate coke deposition, giving the catalyst a lower coke deposition rate and longer lifespan [15,16]. However, the hydrogenation also inevitably leads to excessive hydrogenation of olefins, resulting in a decrease in the selectivity for light olefins. In general, under the high reaction temperature conditions, the catalyst with a stronger acidity always shows a higher selectivity for paraffins, and exhibits a longer lifetime [14–16]. Moreover, due to its thermodynamic favorability, a large amount of CO formation consistently also occurs at high temperatures from the reverse water gas shift reaction during the methanol synthesis step, which can further decrease the yield for light olefins [6]. Recent studies have found that co-feeding water and hydrogen can drastically improve the lifespan of SAPO-34 catalysts, while maintaining olefin selectivity from MTO reactions. Unfortunately, SAPO-34 has been found to suffer serious structural damage after long-term exposure to reaction conditions with high-pressure steam [17]. In addition, structural damages in SAPO-34 it has been observed at low temperature and atmospheric pressure with only the air humidity during ammonia selective catalytic reduction, used for cleaning emissions from vehicles [18]. In view of the fact that a large amount of product water is inevitably produced in the CO₂ hydrogenation reaction, the catalyst requires a certain degree of hydrothermal stability to maintain a high stability. Therefore, it is necessary to optimize the bifunctional catalyst components and the reaction coupling, to reduce the selectivity for CO and paraffins, and in turn boost the olefin selectivity.

SSZ-13 is a zeolitic homologue of the SAPO-34 molecular sieve with the same CHA structure, however with a different framework composition [19]. Comparatively, the SSZ-13 zeolite has better hydrothermal stability [20], and stronger BAS strength [21,22], thus leading to an optimal production rate of olefins at a lower temperature [21]. However, due to the strong acidity, it tends to have a quicker deactivation under pure MTO reaction conditions and exhibit a higher paraffin selectivity during the hydrogenation of CO or CO₂ to olefins [23–25]. In order to increase the selectivity for olefins and improve the stability of catalysts for the MTO reaction, many research efforts have focused on modified properties and treatments of zeolite catalysts, such as an increase of Si/Al ratio in the bulk composition [19,26], steaming treatment [27], or ion exchange with metal ions in post-synthesis [28]. Typically, these modifications were thought to either alter the acidity or alter the pore structure, thereby altering the reactivity and product distribution [13].

Recent research has disclosed that the distribution of the Al atoms in the framework of the SSZ-13 zeolite is another key factor that may affect its catalytic activity and selectivity in MTO reactions [19,27,29,30]. The distribution of Al describes the two different types of proximity of Al atoms in the arrangement [Al-O-(Si-O)_x-Al] in the framework, and they are denoted as isolated ($x > 2$) and paired ($x = 1, 2$) Al species, which also represents isolated BAS and paired BAS respectively [31]. The latter one is distinguished by its ability to exchange divalent cations, such as Co²⁺ and Cu²⁺ [19,31]. By either increasing the Si/Al ratio in the bulk composition to decrease the paired Al on average, or by exchanging with Cu²⁺ to neutralize the paired BAS in the framework, it is claimed that a higher proportion of paired BAS inside SSZ-13 is responsible for hydrogen transfer reactions under pure MTO reaction conditions, which leads to heavy coke formation and high selectivity for propane [19]. Similar reports also found that SSZ-13 zeolite synthesized from FAU-type zeolite, having a high proportion of Q⁴(2Al) [Si(OSi)₂(OAl)₂] structure in the framework, showed a short catalytic life for MTO reactions [29]. Gounder and his colleagues have recently reported a distinct SSZ-13 zeolite only with isolated Al (with isolated proton sites) in the framework, which was synthesized by using the N, N,

N-trimethyl-1-adamantylammonium (TMAda⁺) as the sole structure directing agent (SDA) during crystallization [31]. By comparison with SSZ-13 containing paired Al sites (with paired proton sites) in the structure, they confirmed that the rate constant for methanol dehydration for paired proton sites was 10 times higher than for isolated proton sites [30]. Thus, it is indicated that the distribution of aluminum and its related BAS distribution might play an important role in the product distribution during the process of methanol-intermediated CO₂ hydrogenation into olefins.

Early relevant literature reported that zeolite acidity plays an important role in the combined CO₂ hydrogenation and MTO reactions and revealed the contribution of acid density to the selectivity of products (such as unreacted methanol, alkenes or alkanes) [32]. However, the relationship between the BAS properties (both BAS density and BAS distribution) of the zeolite and stable olefin production has not been clearly understood, especially for SSZ-13 zeolite with varying BAS distribution. SSZ-13 zeolite is known to be very sensitive to rapid coke deposition under high methanol partial pressures [33]. How to adjust its acidity to promote light olefins production while avoiding rapid deactivation requires systematic research, especially targeting its application under low-temperature reaction conditions, where the formation of CO can be decreased based on thermodynamic effects [6,8,34]. In this study, SSZ-13 zeolite with only isolated BAS has been synthesized, and its BAS density has been modified by adjusting the Si/Al in its bulk composition, or by neutralization with sodium ions by ion exchange. All zeolite samples were assembled into the bifunctional catalysts after mixing with In₂O₃, and the effect of acidity on both the olefin distribution and coke deposition is explored during low-temperature CO₂ hydrogenation. For comparison, the SSZ-13 zeolites with the same bulk composition, but containing paired BAS, were synthesized and tested as a reference.

2. Materials and methods

2.1. Preparation of In₂O₃

The preparation of In₂O₃ oxide has been conducted by a coprecipitation method, which has been described in detail elsewhere [34]. Briefly, indium (III) nitrate hydrate has been used as a metal source and dissolved into deionized water to form a 6.5 wt% of In (NO₃)₃ solution. Then an aqueous solution of Na₂CO₃ (9.1 wt%) was added, dropwise into it until the pH of the mixed solution reached 9.2. The resulting mixture was aged for 1 h under magnetic stirring at ambient temperature. After filtering and subsequent washing with deionized water to dispose of Na⁺, the precipitate was dried in a vacuum oven overnight at 60 °C, and subsequently calcinated at 400 °C for 3 h, to obtain the In₂O₃ sample.

2.2. Synthesis of SSZ-13 with isolated Al distribution

The SSZ-13 zeolite with isolated Al distribution was prepared by adapting the procedure described by Gounder [31]. The N, N, N-trimethyl-1-adamantylammonium hydroxide (TMAdaOH, 25 wt%, Tokyo Chemical Industry Co. Ltd.) was used as the structure-directing agent (SDA) during the hydrothermal crystallization, whereas silica sol (LUDOX® AS-40, 40 wt%) and Al(OH)₃ (Sigma Aldrich, >99%) were utilized as the precursors of Si and Al. The composition of the precursor mixture was at a molar ratio of 100SiO₂/aAl₂O₃/50TMAdaOH/4400 H₂O, where 'a = 3.33, 2.5 and 2' represents the Si/Al molar ratios of 15, 20 and 25, respectively. Using a typical synthesis procedure, TMAdaOH was dissolved into deionized water first, then the Al (OH)₃ was added into the TMAdaOH solution to form a homogenous mixture under magnetic stirring at ambient temperature. Next, silica sol (LUDOX® AS-40, 40 wt%) was added to the mixed solution and stirred for 2 h to obtain a precursor gel. This synthesis gel was then put into a 160 ml Teflon-lined stainless-steel autoclave and heated at 160 °C for 6 days of

crystallization under 40 RPM rotation. The resulting zeolite was filtered, washed, and then dried at 110 °C overnight. After subsequent calcination at 600 °C for 8 h under air flow in order to eliminate the residual SDA, the proton type of SSZ-13 zeolite with isolated Al distribution, was obtained and will be denoted as H-ISO-x, here 'x' represents the molar ratio of Si/Al from the designated formulation. Correspondingly, the as-synthesized zeolite containing SDA is referred to TEA-ISO-x.

In order to modify the BAS density of SSZ-13, the ion exchange from proton-typed SSZ-13 was carried out with aqueous sodium nitrate solution, with varying molarities ranging from 0.033 to 2 mol/L, at room temperature. Specifically, 3 g of zeolite sample was ion-exchanged with 300 ml of the designated concentration of NaNO₃ (Sigma Aldrich, > 99%) solution, for 24 h, at 25 °C under stirring. This ion exchange treatment was carried out once without controlling the pH of the solution. Then, the zeolite slurry was filtered, washed three times with deionized water, and subsequently dried at 110 °C overnight. After calcination at 550 °C for 4 h in static air, the obtained sample will be denoted as Na-y-ISO-x, where 'x' represents the molar ratio of Si/Al from the designated formulation, and 'y%' indicates the exchange degree, which was determined by the molar ratio of Na to Al from composition analysis.

2.3. Synthesis of SSZ-13 with paired Al distribution

SSZ-13 zeolite containing paired Al distribution was synthesized in a hydroxide media from a gel precursor, which includes both organic (TMAda⁺) and inorganic cations (Na⁺) as SDAs [19]. Using the fumed silica (fumed powder, 99.8%, Sigma-Aldrich) and Al (OH)₃ (Sigma Aldrich, > 99%) as Si and Al sources, the precursor gel was prepared in a molar composition of 100SiO₂/bAl₂O₃/20TMAdaOH/10Na₂O/4000H₂O, where 'b' was varied for different Al contents from 2, 2.5–3.3. Firstly, the designated amount of NaOH (Sigma Aldrich, ≥98% anhydrous pellets) and TMAdaOH (TMAdaOH, 25 wt%, Tokyo Chemical Industry Co. Ltd.) were mixed well and dissolved into deionized water to form the mixed SDA solution. Then the Al and Si sources were added, and a homogenous precursor gel was made according to the same procedure for the H-ISO-x samples. Next, the precursor gel was transferred to a teflon-lined stainless-steel autoclave and hydrothermal synthesis was carried out at 160 °C with a 40 rpm rotation rate for 4 days. After crystallization, washing, and drying, calcination at 600 °C for 8 h under flowing air followed. The obtained Na-typed SSZ-13 will be named as Na-PAR-x. Afterward, the ion exchange treatment of Na-PAR-x was carried out at 80 °C by using 2.5 M NH₄NO₃ aqueous solution and repeated twice to obtain the NH₄-typed zeolite. After drying and calcination at 550 °C for 4 h in air, the final zeolite sample will be designated as H-PAR-x, where 'x' represents the molar ratio of Si/Al derived from the formulation used.

2.4. Synthesis of cobalt cation-exchanged zeolites

The saturation Co²⁺ exchange capacity was used as a descriptor of the number of paired proton sites inside the proton-type SSZ-13 zeolite [31,35,36]. Prior to characterization, the proton-type zeolite samples were first subjected to Co²⁺ ion exchange in an aqueous solution, followed by a rehydration treatment [35]. In a typical aqueous-phase ion exchange of Co²⁺ with the proton type SSZ-13 zeolites, 1 g of proton type of SSZ-13 zeolite powder was mixed well with 150 ml of 0.5 M cobalt (II) nitrate (Sigma Aldrich, ≥98%) solution under stirring. After ion exchange at 80 °C for 48 h, the solid phase was collected by centrifugation and washed 4 times with deionized water, then the resulting sample was dried overnight at 110 °C and calcined at 500 °C for 1 h in static air. After ion exchange, the sample was first impregnated in an equal volume of deionized water for 1 h, and then dried at 100 °C for 3 h to achieve rehydration. The final obtained sample will be denoted as Co-ISO-x or Co-PAR-x respectively, where 'x' also represents the molar ratio of Si/Al derived from the designed formulation.

2.5. Preparation of bifunctional catalysts

The bifunctional catalysts (denoted as M/H-ISO-x, M/Na-y-ISO-x or M/H-PAR-x) were prepared by physically mixing the granules of In₂O₃ oxide and the SSZ-13 zeolite sample (such as H-ISO-x, Na-y-ISO-x, or H-PAR-x). The weight ratio of the two ingredients was fixed at 2:1 in the present study. In order to compare with the tandem catalysts, the same amount of indium oxide catalyst was mixed with inert silicon carbide to form the pure indium oxide catalyst, denoted as M(In₂O₃).

Briefly, for physical mixing, the sample powders of In₂O₃ and SSZ-13 were pressed separately, then crushed, and sieved into granules using the size range of 250–500 μm. Thereafter, these two granular components were mixed homogeneously by shaking in a glass vessel.

2.6. Characterization of fresh bifunctional catalysts and individual components

The X-ray diffraction pattern of zeolite and oxides were measured by using a Bruker D8 X-ray diffractometer with CuKα (λ = 1.54 Å) radiation. The elemental composition (Si, Al and Na) of all samples was measured using a wavelength dispersive X-ray fluorescence (WDXRF) spectrometer (Zetium, Malvern-Panalytical) equipped with a Rh anode as the X-ray source. The trace amount of cobalt inside the Co²⁺-exchanged sample was determined by using inductively coupled plasma sector filed mass spectrometry (ICP-SFMS) in the lab of ALS Scandinavia AB (Luleå, Sweden). Scanning electron microscopic (SEM) images of powder samples were obtained on a JEOL JSM-7800 F scanning electron microscope. The specific surface area and pore volume of samples were determined by N₂ adsorption at −196 °C on a Micromeritics Tri-Star 3000 instrument. Samples were degassed at 300 °C for 6 h prior to measurements. The total surface area was determined using the Brunauer Emmett Teller (BET) method, and the micropore volumes were determined using the t-plot method.

²⁷Al MAS NMR, ²⁹Si MAS NMR and ²⁹Si CP MAS NMR spectra were obtained on a Bruker Avance III 500 MHz NMR spectrometer equipped with a 4 mm double-resonance MAS probe. The ²⁷Al single pulse spectra with high power decoupling spectra (hpdec) were recorded at 130.3 MHz with a MAS spinning rate of 11 kHz. Scans were collected at room temperature by using a radio frequency pulse of 4 μs corresponding to a 60-degree excitation, followed by 5 ms acquisition under 66 kHz ¹H SPINAL64 decoupling with a relaxation delay of 0.5 s. The single pulse ²⁹Si MAS NMR spectra were acquired at 99.4 MHz with a MAS spinning rate of 11 kHz, and a pulse of 3 μs was used for excitation (45°) with 10 ms acquisition under 50 kHz ¹H SPINAL64 decoupling and a relaxation delay of 5 s. The ²⁹Si cross-polarization (CP) MAS NMR spectra were collected by employing a cross-polarization pulse sequence with 5 ms of contact time and 2 s of recycle delay. All chemical shifts were referenced externally to the methylene (−CH₂−) group of adamantane set to 38.48 ppm (with sr = 0). The framework Si/Al ratio of the zeolite sample was estimated by using the reported equation as below [29,35]:

$$\frac{Si}{Al} = \frac{\sum_n^4 I_{Q4(nAl)}}{I_{Q4(4Al)} + 0.75 * I_{Q4(3Al)} + 0.5 * I_{Q4(2Al)} + 0.25 * I_{Q4(1Al)}}$$

Where n is the number of O-Al bindings with Si, and the $I_{Q4(nAl)}$ is the integrated peak area from ²⁹Si MAS NMR spectra corresponding to each Si with different Q⁴(nAl) [Si(OSi)_{4-n}(OAl)_n] coordination.

The UV-Vis diffuse reflectance (DRS UV-vis) spectra of cobalt ion-exchanged zeolites were collected on a LAMBDA 365 UV-Vis Spectrophotometer (PerkinElmer) with an integrating Reflectance sphere accessory (50 mm) attachment. Before the characterization, the sample was calcined at 550 °C under the static air for 1 h, and subsequently rehydrated at 110 °C. The baseline was recorded by using BaSO₄ (Sigma Aldrich, ≥98%) as 100% reference. Then the rehydrated sample was packed in the Quartz powder cell, and the spectrum was collected from

10000 to 40000 cm⁻¹ with a scan rate of 240 cm⁻¹/s. The diffuse reflectance was transformed into absorption intensity by using the Schuster-Kubelka-Munk equation: $F(R_{\infty}) = (1 - R_{\infty})^2 / 2R_{\infty}$, where R_{∞} is the diffuse reflectance from a semi-infinite layer [36].

The *In-situ* diffuse reflectance infrared Fourier transform spectra (DRIFTS) were collected using an FT-IR spectrometer (Vertex 70, Bruker) equipped with a mercury cadmium telluride (MCT) detector and a diffuse reflectance accessory (Thermo Scientific™). The sample powder was loaded into a high-temperature reaction cell (Harrick Praying Mantis) with a CaF₂ window. The temperature of the cell was regulated by a Eurotherm 2416 controller, and the gas flow and composition through the cell was controlled by mass flow controllers (Bronkhorst). Prior to the experiment, each sample was pretreated at 550 °C for 60 min under 100 ml/min of Ar flow, then cooled down to 30 °C. After collecting the spectra of the sample hydroxyl groups at 30 °C under Ar flow, the sample was exposed to 1000 ppm of NH₃ in Ar flow (100 ml/min) for 1 h at 30 °C. The low temperature (30 °C) adsorption spectra were continuously recorded until the sample reached adsorption saturation. This saturation of the sample was confirmed with a mass spectrometer (Hiden HR20) connected to the outlet stream of the cell. In order to remove the weakly adsorbed ammonia, the sample was heated from 30 °C to 200 °C under Ar flow for desorption, and then cooled down to 30 °C for the high temperature (200 °C) adsorption spectra collection. All of the spectra were collected over 4000–1000 cm⁻¹ with a resolution of 4 cm⁻¹.

Temperature-programmed desorption of ammonia (NH₃-TPD) measurements were carried out on a calorimeter (Sensys DSC, SETARAM) coupled with a mass spectrometer (HPR-20 QUI, Hiden). Typically, 30 mg of granular sample (250–500 μm) was placed into a quartz tube reactor and pretreated at 550 °C for 1 h in flowing Ar (500 ml/min), then cooled to 100 °C. Thereafter, a 2000 ppm of NH₃/Ar flow with a flow rate of 20 Nml/min was introduced into the reactor and maintained for 2 h until saturation was reached, afterwards it was flushed using flowing Ar (20 Nml/min) for 4 h, in order to remove the physisorbed NH₃. The desorption of NH₃ was performed by increasing the temperature from 100 °C to 700 °C with a ramping rate of 10 °C/min under a pure Ar (20 Nml/min) flow. The desorbed NH₃ was monitored by an online mass spectrometry, where the concentration of NH₃ was recorded at the characteristic mass to charge ratio (m/z) at 17, and the intensity of the signal was calibrated by using gas mixtures prior to the experiment.

2.7. Catalytic performance tests

The CO₂ hydrogenation was performed on a high-pressure fixed bed flow reactor (VINCI Technologies, France) equipped with a stainless-steel tube (i.d. 8.3 mm × L 215 mm). The reaction temperature was monitored by a K-type thermocouple with its tip positioned in the center of the catalyst bed, and the reaction pressure was controlled automatically by a pneumatic back pressure valve. In a typical run, 1 g of bifunctional catalyst was packed into the reactor tube and was pretreated under Ar flow (150 Nml/min) at 400 °C for 1 h at ambient pressure prior to the reaction. After the catalyst bed was cooled down to 325 °C in pure Ar, the reactant gas mixture, with a H₂/CO₂ ratio of 6, was introduced into the reactor at a gas hourly space velocity (GHSV) of 6400 NML·g⁻¹·h⁻¹. The reaction started when the pressure was raised to the required reaction pressure of 10 bar. The compositions of reactants and effluent gas were continuously analyzed by an online gas chromatograph (GC-456, Bruker) equipped with a flame-ionized detector (FID), and a thermal conductivity detector (TCD). The CO₂ conversion, the CO and Methanol selectivity, and the selectivity of individual hydrocarbon products, excluding CO, were calculated according to the equations as below.

CO₂ conversion :

$$\text{Conv.CO}_2 = (n_{\text{CO}_2,\text{in}} - n_{\text{CO}_2,\text{out}}) / n_{\text{CO}_2,\text{in}} * 100\%$$

CO selectivity :

$$\text{Sel.CO} = n_{\text{CO}} / (n_{\text{CO}_2,\text{in}} - n_{\text{CO}_2,\text{out}}) * 100\%$$

CH₃OH selectivity :

$$\text{Sel.MeOH} = n_{\text{MeOH}} / (n_{\text{CO}_2,\text{in}} - n_{\text{CO}_2,\text{out}}) * 100\%$$

Dimethylether (DME) selectivity :

$$\text{Sel.DME} = 2 * n_{\text{DME}} / (n_{\text{CO}_2,\text{in}} - n_{\text{CO}_2,\text{out}}) * 100\%$$

C_nH_m selectivity among hydrocarbons excluding CO, CH₃OH and DME:

$$\text{Sel.C}_i\text{H}_j = i * n_{\text{C}_i\text{H}_j} / (n_{\text{CO}_2,\text{in}} - n_{\text{CO}_2,\text{out}} - n_{\text{CO}} - n_{\text{MeOH}} - 2 * n_{\text{DME}}) * 100\%$$

Where $n_{\text{CO}_2,\text{in}}$ refers to the moles of CO₂ at the inlet, and $n_{\text{CO}_2,\text{out}}$, n_{CO} , n_{MeOH} , n_{DME} , $n_{\text{C}_n\text{H}_m}$ represents the moles of the CO₂, CO, CH₃OH, DME, and individual hydrocarbons at the outlet, respectively.

2.8. Analysis of coke species inside the spent catalyst

After the reaction, the spent catalyst was cooled to room temperature by argon purging overnight, then taken out and ground into a uniform powder. To obtain the content of the retained coke inside the catalysts, the thermogravimetric analysis (TGA) was conducted using a Thermal Analysis System TGA/ DSC 3 + (Mettler Toledo). Typically, 10 mg of spent catalyst was packed in an alumina crucible and was heated to 700 °C, with a ramping rate of 10 °C/min in an air flow of 100 ml/min. The amount of coke was estimated from the weight loss between 300 °C and 700 °C.

The detailed components of the soluble coke were analyzed by using the method described by Bhawe et al. Approximately, 100 mg of the spent catalyst powders were firstly digested in 2 ml of HF solution (48 wt%) for 30 min to recover the encapsulated hydrocarbons, then these hydrocarbons were extracted by adding 5 ml of dichloromethane (CH₂Cl₂). After filtering, 1 μl of the obtained organic liquid mixtures were injected into a gas chromatography/mass spectrometry system (GC-MS, Agilent GC 7890B, Agilent 5977 A mass) equipped with a moderately polar VF1701ms column (30 m × 0.25 mm × 0.25 μm). The injector port temperature was at 280 °C, and the oven was heated from 40 °C to 280 °C at a rate of 10 °C /min and held at 280 °C for 10 min. The total ion current (TIC) chromatograms were obtained via automatic scanning in the range of m/z from 40 to 300. For comparison, each sample was batch injected through an autosampler while maintaining the same injection temperature and the same analysis method.

Temperature-programmed oxidation (TPO) measurements were conducted to distinguish the type of coke trapped inside catalysts. 50 mg of a spent catalyst sample was packed into a quartz tube reactor of the calorimeter-Mass spectrometer system (Sensys DSC, HPR-20 QUI), and was dehydrated at 110 °C for 1 h then cooled down to 25 °C in flowing Ar (20 Nml/min). Thereafter, 5000 ppm of O₂/Ar flow (20 Nml/min) was introduced and maintained for 30 min until the baseline of oxygen MS signal (m/z = 32) was stable. Further, the sample was heated from 25 °C to 700 °C (10 °C/min) and held at 700 °C for 2 h in order to completely decompose all organics. The MS signals of outlet O₂ (m/z = 32), CO₂ (m/z = 44), CO (m/z = 28) and H₂O (m/z = 18) were monitored as a function of time on stream (TOS). The intensities of these gas signals were calibrated by using the known gas mixtures prior to the experiment.

3. Results and discussion

3.1. Bulk properties of two types of SSZ-13 zeolites

The structural properties of the two types of SSZ-13 are shown in Table 1, where H-PAR-x (includes sodium in the gel during synthesis) has more paired Al-sites, whereas H-ISO-x (no sodium in the gel) contains almost only isolated Al-sites. To ensure that the sodium-free gel systems can produce pure CHA structures, and investigate the effect of Na⁺ on the crystallization of SSZ-13 zeolite, the Si/Al ratio (SAR) of the

Table 1

Characterization results of two series of proton-type SSZ-13 zeolite samples with different Si/Al ratios.

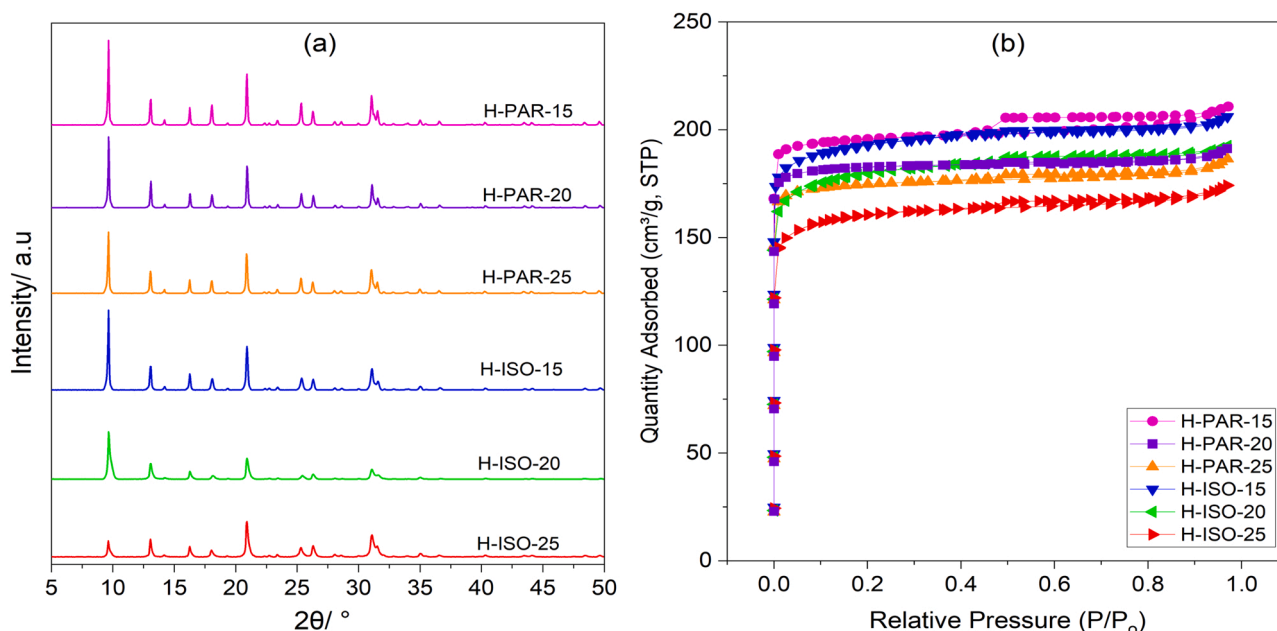
Sample	Si/Al ratio ^a	RC ^b	S _{BET} ^c /m ² g ⁻¹	V _{meso} ^d /cm ³ g ⁻¹	V _{micro} ^e /cm ³ g ⁻¹	Particle size ^f /μm	Particle shape ^g	Co ²⁺ exchange capacity ^h
H-PAR-15	13.9	100.0%	622.3	0.042	0.28	0.84	cube	0.12
H-PAR-20	20.2	87.7%	581.0	0.025	0.27	3.93	cube	0.11
H-PAR-25	26.5	82.7%	556.1	0.033	0.26	4.19	cube	0.09
H-ISO-15	14.2	99.1%	617.7	0.056	0.26	2.73	pseudo-cube	0.02
H-ISO-20	20.3	56.0%	578.3	0.059	0.24	2.88	cube	< 0.01
H-ISO-25	27.3	35.6%	514.8	0.051	0.22	2.84	cube	< 0.01

^a Mole ratio was determined by XRF.^b Relative crystallinity (RC) was calculated from an earlier reported method [37]: $RC_x = \sum I_x / \sum I_0 \times 100\%$, where $\sum I_x$ is the sum of the XRD diffraction peak areas of sample x at $2\theta = 9.6^\circ$ and 20.9° , where $\sum I_0$ is the sum of the XRD diffraction peak areas of sample H-PAR-15 at $2\theta = 9.6^\circ$ and 20.9° .^c BET surface area was measured from N₂ adsorption isotherm using the BET method.^d Mesopore volume was measured from N₂ adsorption isotherm using the BJH method.^e Micropore volume was measured from N₂ adsorption isotherm using the t-plot method.^f Average crystal particle size was estimated from SEM micrographs.^g Crystal particle shape was also estimated from SEM micrographs.^h Cobalt cation exchange capacity was calculated based on the mole ratio of Co to 2Al (n_{Co}/n_{2Al}) inside of Co-exchange samples, the concentrations of Co and Al were obtained from the ICP-SFMS results (Table S1, Supplementary material).

gels was set equally, between 15 and 30 [31]. The XRD patterns and the N₂ adsorption–desorption isotherms (−196 °C) of the two types of HSSZ-13 samples are shown in Figs. 1a and 1b. The results indicate that all samples exhibited the diffraction peaks characteristic of the CHA framework topology [38], and they had microporous structures with typical type I isotherms [19,31]. The micropore volumes of these samples were either higher than, or close to, the pore volume of the theoretical CHA topology ($0.24 \text{ cm}^3 \text{ g}^{-1}$) [35]. The XRD patterns of all samples (Fig. 1a) had the same crystal plane orientation except for sample H-ISO-25. This is manifested by nearly the same ratio of two peak intensities at 2θ values of 9.6° and 20.9° , corresponding to the (110) and (210) crystal planes [38]. In order to evaluate the crystallinity of the samples, the areas of peaks at $2\theta = 9.6^\circ$ and 20.9° were integrated, and the sum of the areas of these corresponding peaks in sample H-PAR-15 was assigned as 100% of relative crystallinity. The results of relative crystallinity demonstrate that the sodium ions and the SAR of the gel precursor have important effects on the crystallization of SSZ-13 zeolites. In the synthesis using both Na⁺ cations and TMAda⁺ as SDAs, after 96 h of hydrothermal crystallization, the SSZ-13 zeolites (H-PAR-x) with good crystallinity were successfully obtained. Moreover, their

relative crystallites had only decreased slightly, with an increase in Si/Al. For the other case TMAda⁺ was used as the sole SDA. After 144 h of crystallization, at a SAR of 15, the resulting sample, H-ISO-15, had a comparative crystallinity to the sample H-PAR-15, which was synthesized using both Na⁺ and TMAda⁺ as SDAs. However, as the SAR increased from 15 to 25, the crystallinity significantly declined, and the relative crystallinity dropped to 36%. Correspondingly, the micropore volume also decreased to $0.22 \text{ cm}^3 \text{ g}^{-1}$, and the BET surface area decreased to $514.8 \text{ m}^2 \text{ g}^{-1}$.

The SEM images of all H-SSZ-13 samples are shown in Fig. 2. The SSZ-13 zeolites synthesized using Na⁺ and TMAda⁺ cations as SDAs had a cubic morphology in a SAR range from 15 to 25. The sample H-PAR-15 exhibited the smallest crystal particle size ($0.84 \mu\text{m}$ on average) without aggregation (Fig. 2a). The resulting SSZ-13 zeolites in the system containing only TMAda⁺ cations as an SDA exhibited diverse morphologies. The sample H-ISO-15 had pseudo-cubic crystal particles with rounded edges, however, the macro steps appeared on one crystal surface (Fig. S1, a), which looked like the aggregate of small and layered crystals. As the SAR increased, the crystal particles of the sample gradually turned to cubic shape, and the sample H-ISO-25 showed facets of cubic

**Fig. 1.** XRD patterns (a) and N₂ adsorption-desorption isotherms (b) of synthesized H-ISO-x and H-PAR-x samples (x = 15, 20, 25).

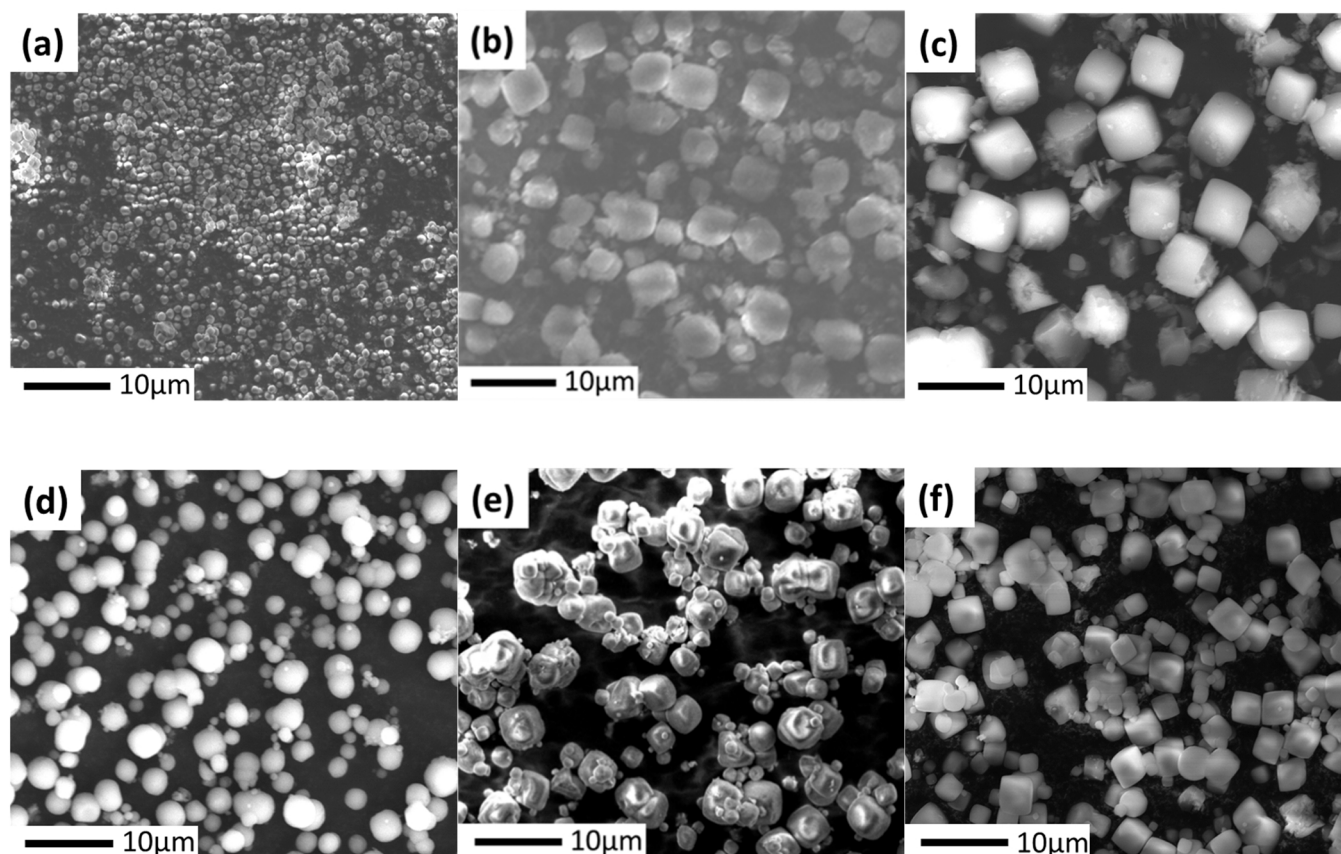


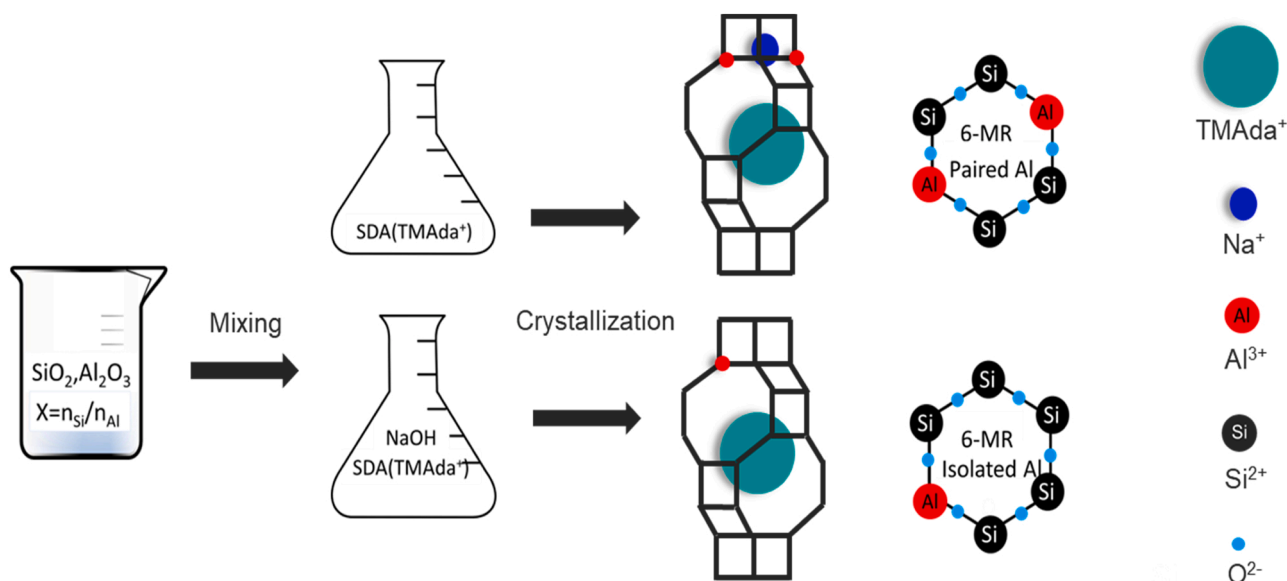
Fig. 2. SEM images of two types of HSSZ-13 zeolites: (a) H-PAR-15, (b) H-PAR-20, (c) H-PAR-25, (d) H-ISO-15, (e) H-ISO-20, (f) H-ISO-25.

crystal particles (Fig. 2f). Notably, there were no irregular silicon-aluminum oxides or worm-like amorphous precursors on the crystal surface of sample H-ISO-20 (Fig. S1, b) or H-ISO-25 (Fig. S1, c), although the XRD and nitrogen adsorption experiments showed that the crystallinity of these samples were lower.

The SSZ-13 zeolite has been reported to follow two potential pathways for crystallization: One is to follow the layer-by-layer mechanism, where the dissolution of the precursor and the re-growth of the crystal, usually leading to a well-defined cubic phase crystal. The other is the particle-intermediated growth pathway, in which the precursors first form crystals with irregular shapes and rough surface features through the attachment and reconstruction of the crystal nucleus, and then these crystals ripen into cubic crystals [39]. A few works also found that spherical crystals of SSZ-13 with rough surfaces were also present in Na⁺-containing systems [26,39,40], and the longer the crystallization time was, the more cubic the crystals were [39,40]. This demonstrates that the crystal morphology is not closely related to the composition of the SDAs in the synthesis system but is directly related to the degree of maturation in crystallization. In all pathways of crystallization, compared to samples with higher SAR, the precursor of the sample with a lower SAR ratio contained more [AlO₄]⁻ tetrahedra, and it took a longer time to crystallize into the zeolite framework. Therefore, within a certain synthesis time, the degree of ripening may be low, which resulted in aggregated or discrete small grains, such as for sample H-ISO-15 and H-PAR-15.

In comparing the two synthesis methods, with and without Na⁺ cations as an SDA, it was found that Na⁺ cations not only significantly affected the crystallization rate of the SSZ-13 zeolite, but also affected the crystallinity of the SSZ-13 zeolite. Na⁺ cations are generally considered to enhance the rate of crystallization of zeolites by promoting the polymerization and dissociation of precursors [35]. Therefore, the short crystallization time (96 h) was adopted for the synthesis method

containing sodium cations as an SDA. In contrast, using the synthesis method without Na⁺ cations, the crystallization time needed to be extended to 144 h. Unfortunately, even with this longer crystallization time, without the help of Na⁺ cations, it was still difficult to synthesize SSZ-13 zeolite with good crystallinity when the precursor had a relatively high Si/Al ratio. Gounder. et al. confirmed that it was difficult to synthesize crystalline SSZ-13 zeolite with a SAR value of less than 15 or greater than 30 in an alkaline gel system containing only TMAda⁺ as an SDA and speculated that this was the result of the exogenous TMAda⁺ cations being occluded within the cage of crystalline SSZ-13 during crystallization [30,31]. The sodium cation has a smaller ionic radius and cationic charge density than the organic structure-directing agent TMAda⁺. As a result, the amount of sodium and TMAda⁺ cations affect the anionic charge density on the zeolite lattice during crystallization. For the synthetic system with or without Na⁺ included in the SDA, the distribution of framework aluminum can be illustrated as Scheme 1. In the case of TMAda⁺ as the sole SDA, the size of TMAda⁺ (0.7 nm in diameter) and corresponding steric constraints restrict each CHA cage (0.72 nm in diameter) to be occupied by only one TMAda⁺ molecule [30]. Thus, a single cationic charge of TMAda⁺ imposes an electrostatic constraint, placing an anionic framework Al in the lattice. Therefore, the distance between the resulting framework Al atoms will be relatively far, which we shall call isolated Al. In contrast, in the presence of both Na⁺ and TMAda⁺ as SDA, more intimate contact framework Al atoms (paired Al) can be allowed since the extra anionic charge of [AlO₄]⁻ can be balanced by the small sodium cation. Moreover, if the TMAda⁺ cations have been the sole cations in the system, they are capable of balancing the limited anionic charge generated by [AlO₄]⁻ tetrahedrons in the framework. Hence, the composition (SAR of the framework) of the crystalline SSZ-13 zeolite is fixed in a narrow range. In accordance with the charge density mismatch theory [31], when the Si/Al is less than 15, and there is a lack of free cations (such as Na⁺ cations) in the system, due



Scheme 1. The framework Al distribution during the crystallization of SSZ-13 zeolites with or without Na⁺ in the SDA. lines denote Si-O-Al-O-Si or Si-O-Al-Si linkages in framework, and red dots denote Al³⁺ substitutions. TMAda⁺ and sodium cations are represented as turquoise and blue spheres, respectively.

to the limitation of charge balance, the [AlO₄][−] tetrahedrons that are far away from TMAda⁺ cations cannot be generated normally in the framework. Therefore, the crystallization of the CHA topology is strained, resulting in amorphous phases, or miscellaneous crystals with other topologies being formed. When the Si/Al is greater than 30, the content of aluminum is low, and the formation of [AlO₄][−] tetrahedron with anionic charge is decreased. Therefore, the occluded TMAda⁺ cations in the eight-membered rings generate excessive cationic charges that need to be balanced. At this time, anion framework vacancy defect ([S-O][−]) sites are forced to form, and thus the crystallization process is also affected [30]. When the SAR of the precursor was in the range of 15–30, the aluminum atoms in the framework could concentrate near the TMAda⁺ cations to balance their charges, thus the isolated framework aluminum is produced. In the synthesis procedure used here, although the valid SAR range (15–25) was used to synthesize SSZ-13 zeolite, it was found that the crystallinity decreased drastically with an increase in the SAR. It is worth noting that no miscellaneous crystals or amorphous silicon-alumina were found using XRD or SEM, which indicates that the framework defect sites may have been generated, resulting in a decrease in crystallinity.

3.2. Identification of Al environment inside SSZ-13 zeolites

To gain insight into the structure of the two types of H-SSZ-13 zeolites, and specifically into the silico-alumina chemical environment related to acid distribution and acid strength, the ²⁷Al (MAS) and ²⁹Si (MAS and CP-MAS) NMR spectra were collected, and are shown in Fig. 3. The ²⁷Al MAS NMR spectra of sample H-PAR-x (x = 15, 20, 25) and sample H-ISO-x (x = 15, 20, 25) exhibited different ²⁷Al NMR resonances at 60 and 0 ppm (Fig. 3a). The resonance at approximately 60 ppm was assigned to the tetrahedrally coordinated Al atoms in the framework, and the signal at 0 ppm was attributed to the extra-framework octahedrally coordinated Al atoms [29,31,35,41,42], two small peaks around 145 ppm and −25 ppm are attributed to spinning sidebands that result during the data collection [43]. It can be seen that nearly all of the aluminum atoms in the H-PAR-x samples were in the framework. In contrast, extra-framework aluminum species were generated in the H-ISO-x samples, which is in line with the lower crystallinity found for the ISO samples.

The ²⁹Si MAS spectra of all H-SSZ-13 samples are shown in Fig. 3b (solid traces), giving two distinct resonance peaks at approximately

−111 ppm and −104 ppm. The ²⁹Si MAS resonance at −110 ppm is usually identified for the Si atom in the Q⁴(0Al) configuration, and the one at approximately −104 ppm can be assigned to Q⁴(1Al) since the replacement of one Si by one Al atom in the framework of zeolite causes a downfield shift of about 5 ppm [29,31,35,41,42]. For a broad resonance peak centered at −100 ppm, it could originate from either the Si atom in Q⁴(2Al) or Q³(0Al) configurations [31,42]. However, this peak was enhanced when the cross-polarization (²⁹Si CP-MAS in Fig. 3b, dotted traces) was applied. Because the silanol groups could enhance Si resonance signals during cross-polarization, it is reasonable to speculate that the peak at −100 ppm is mainly attributed to the resonance of Si atom in the Q³(0Al) [Si (OSi)₃(OH)] coordination, rather than in Q⁴(2Al) [Al-O-Si(OSi)₂-O-Al].

Based on the identification of the above-mentioned resonance peak positions, curve fitting was performed on the ²⁹Si MS NMR spectra, and the estimated Si/Al ratios in the zeolite frameworks were calculated based on relative peak areas, as shown in Table 2. The framework Si/Al ratios (SAR) of the proton-type zeolite H-PAR-x samples (synthesized using both Na and TMAda⁺ as SDAs, followed by ion exchanging with NH₄⁺ and calcination) estimated from the ²⁹Si MAS NMR experiment were in agreement with the results obtained from XRF measurements. This indicates that the aluminum source was effectively introduced into the framework of the zeolite, which was also consistent with the results obtained from the ²⁷Al MAS NMR and XRD. However, for the proton-type zeolite H-ISO-x samples (synthesized using TMAda⁺ as a sole SDA, followed by calcination), their SAR values in the framework were consistently much higher than the bulk phase values, and this discrepancy is apparently due to the distinct non-framework Al species detected in the ²⁷Al spectra.

In order to explore the origin of the non-framework aluminum and understand the high SAR in the framework of the H-ISO-x samples, two precursor samples of TEA-ISO-x (containing the SDA before calcination, x = 15, 20) were prepared to carry out the ²⁷Al MAS, ²⁹Si MAS, and ²⁹Si CP-MAS NMR analysis. The results are shown in Figs. 3c and 3d. Unlike the samples after calcination (Figs. 3a and 3b), the precursors containing SDA exhibited tetrahedrally coordinated Al (58 ppm) atoms in the framework without any extra-framework aluminum species (Fig. 3c). This showed that the hydrothermal synthesis experiments were successful, and that no unreacted amorphous silica-alumina species existed. Due to the adsorption of SDA cations on the zeolite framework in the zeolite precursors containing SDA, the proton decoupling was enhanced

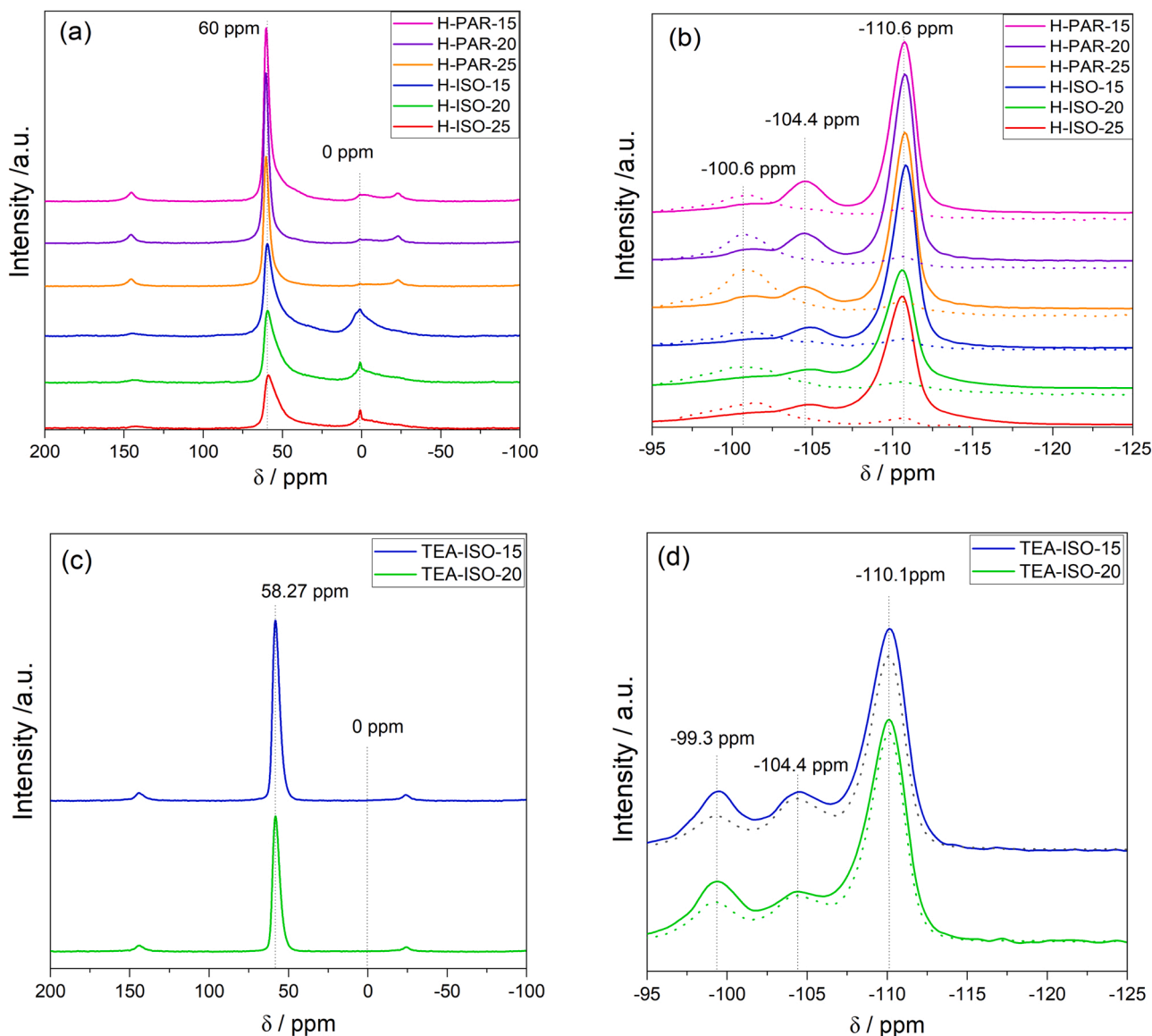


Fig. 3. ^{27}Al MAS (a), ^{29}Si MAS (b, solid traces) and ^{29}Si CP-MAS NMR (b, dotted traces) of proton type of SSZ-13 zeolite samples, and the corresponding ^{27}Al (c) and ^{29}Si NMR (d) resonance spectra of precursor sample TEA-ISO-15 and TEA-ISO-20.

for all Si atoms with different coordination. Therefore, both the ^{29}Si CP-MS spectra and the ^{29}Si MAS spectra displayed three distinct resonance peaks at approximately -110 , -104 , and -99 ppm without any variation (Fig. 3d). As discussed above, there were steric hindrance and charge mismatch effects during the synthesis using solely TMAda⁺ [31], which could make it difficult to generate $[\text{Al-O-Si}(\text{OSi})_2\text{-O-Al}]$ structures with paired Al distribution. Thus, it was still reasonable to assign the resonance peak at -99 ppm to $\text{Q}^3(\text{OAl})$ rather than $\text{Q}^4(2\text{Al})$ linkages. By fitting the curve of ^{29}Si MAS spectra, the results showed that the estimated SAR of the framework were consistent with the results from the bulk phase analysis (in Table 2). These results further confirm that the TEA-ISO-x samples sufficiently preserved the framework before calcination, similar to the results from the ^{27}Al spectra. Also, this indirectly demonstrates that a large number of silanol groups within the $\text{Q}^3(\text{OAl})$ linkages were preserved in the TEA-ISO-x samples. By comparing the ^{29}Si spectra of the samples before and after calcination, it was furthermore found that the resonance peaks related to the silanol structure $\text{Q}^3(\text{OAl})$ (-99.3 ppm) decreased rapidly after calcination and removal of the SDA, which suggests that silanols were potentially the defect sites leading to the collapse of parts of the framework during

calcination. As mentioned in the previous section, in a synthesis system lacking sodium ions, the hydroxyl defect sites are readily formed in zeolites to balance charges caused by TMAda⁺ cations. The higher silicon-aluminum ratio in the precursor, the greater the number of defect sites that are formed. As a result, the TEA-ISO-20 sample should have more defects [$\text{Q}^3(\text{OAl})$] than TEA-ISO-15. This hypothesis has also been confirmed by the deconvolution results from spectra of ^{29}Si MAS NMR, as shown in Table 2.

It has been reported that there are possibly Al-O-Si-O-Al or Al-O-Si-O-Si-O-Al structures in the 6-membered ring of SSZ-13 zeolites, which are called paired Al arrangements [31,41]. With the aid of ^{29}Si MAS and ^{29}Si CP-MS NMR resonance spectroscopy, the existence of Al-O-Si-O-Al [$\text{Q}^4(2\text{Al})$] linkages in the framework of the sample have been ruled out. To further identify whether there were Al-O-Si-O-Si-O-Al linkages as paired Al arrangements, Co^{2+} cation exchange experiments were performed, and the characterization of the related samples was carried out by means of ultraviolet-visible (Uv-Vis) spectrophotometry. It is widely accepted that the pairs of Al atoms in the framework of zeolite can accommodate one bare Co^{2+} cation with tetrahedral coordination in the dehydrated condition and can also uptake the Co^{2+} hexaaqua complexes

Table 2

The deconvolution results of ²⁹Si MS NMR spectra of proton-type SSZ-13 zeolite samples and their corresponding acid amount from NH₃-TPD results.

Samples	Si/Al ^a /100%	Proportion of Q ⁴ (nAl) and Q ³ (nAl) / %				Si/Al ^c /100%	BAS density ^d /mmol·g ⁻¹
		Q ⁴ (0Al)	Q ⁴ (1Al)	Q ⁴ (2Al)	Q ³ (0Al)		
H-ISO-15	13.9	74.5	18.5	0	7.0	20.1	0.35
H-ISO-20	20.2	74.6	13.6	0	11.8	25.9	0.25
H-ISO-25	26.5	72.6	10.5	0	16.9	31.6	0.23
H-PAR-15	14.2	69.4	22.2	0	8.4	16.5	0.41
H-PAR-20	20.3	73.6	18.7	0	7.6	19.7	0.35
H-PAR-25	27.3	74.1	13.3	0	12.6	26.3	0.30
TEA-ISO-15	13.9	61.2	19.0	0	19.9	16.9	/
TEA-ISO-20	20.2	60.0	14.9	0	25.4	20.1	/

^a Mole ratio of Si/Al in bulk phase was determined by XRF.

^b Proportions of the different Si species with the Q⁴(nAl) or Q³(nAl) configurations estimated from ²⁹Si MAS NMR spectra (detailed results of deconvolutions are listed in Fig. S2, Fig. S3 and Fig. S4, Supplementary material), where the Q⁴(nAl) was in the Si (OSi)_{4-n}(OAl)_n coordination, the Q³(nAl) was in the Si (OSi)_{3-n}(OH)(OAl)_n coordination.

^c The Si to Al ratio in the framework was calculated by the equation: $Si/Al = \sum_{n=0}^4 I_{Q4(nAl)} / [I_{Q4(4Al)} + 0.75 * I_{Q4(3Al)} + 0.5 * I_{Q4(2Al)} + 0.25 * I_{Q4(1Al)}]$, where $I_{Q4(nAl)}$ is proportional to Si species with Q⁴(nAl) configuration.

^d Brønsted acid density accessed from the deconvolution of NH₃-TPD curve peaks with centers ranging from 300 °C to 700 °C (detailed results of deconvolutions are listed in Fig. S5 to Fig. S6, Supplementary material).

with octahedral coordination under a humid environment [35,36]. By using Co²⁺ ion exchange, calcination, and subsequent rehydration, the octahedrally coordinated Co²⁺ ions are clearly identifiable. These are taken up by the paired Al atoms in the framework, rather than the cobalt silicate and cobalt oxide, etc [35].

In Fig. 4 (whole spectrum in Fig. S7, Supplementary material), it is clear that a distinct adsorption spectrum centered at approximately

19457 cm⁻¹ (513 nm of wavelength) was present in the rehydrated Co-PAR-x (x = 15, 20, 25) samples, which is attributed to the characteristic absorption band of the d-d electronic transition of octahedrally coordinated Co²⁺ cations [31,35,36]. In contrast, the same absorption band of the Co-ISO-x samples was weak and almost negligible. The elemental analysis from ICP further demonstrated that almost no Co²⁺ cations were exchanged into the H-ISO-x samples (In Table 1). The results of the incorporation of Co²⁺ cations in the framework, however confirmed the presence of paired Al coordination in the proton-type H-PAR-x samples. In contrast, the H-ISO-x samples could not exchange Co²⁺ cations, however they did take up the Na⁺ cations (detailed results can be seen in the NH₃-TPD results in the following section), which demonstrates that they contained only isolated Al atoms. These results also showed that the synthesis was successful. According to the mechanism proposed by Gounder. et al. [31], in the synthetic system without free Na⁺ cations, one of the restricted TMAda⁺ cations can only balance one negative charge generated by an [AlO₄]⁻ tetrahedron. Therefore, the isolated Al sites were formed in the framework. When there were enough free Na⁺ cations in the precursor, the negative charges generated by the framework alumina tetrahedrons could easily be balanced by Na⁺ cations without steric limitation, therefore the paired Al atoms were formed in the framework. In general, the less Al resource in the precursor, the fewer pairs of Al atoms were formed. Thus, with an increase in the SAR ratio, the saturation exchange capacity of Co²⁺ cation was decreased and the intensity of corresponding UV-Vis peak (at 19457 cm⁻¹) became weaker in the Co-PAR-x samples.

3.3. Acidity characterization

The in-situ IR spectroscopic experiments were carried out to obtain information on the surface acidity of the two types of H-SSZ-13 zeolites. After pretreatment at 550 °C in Ar, the hydroxyl bands of zeolites were observed in all proton-type samples, and none of the Al-OH (approximately 3782 cm⁻¹) band attributed to amorphous alumina [44] was found in all samples as shown in Fig. 5a. The band at 3735 cm⁻¹ is attributed to the silanol group, while the broad bands from 3612 cm⁻¹ to 3585 cm⁻¹, are ascribed to the bridged OH groups (Si-OH-Al), which are often correlated with Brønsted acid sites in the framework [44–46]. In terms of the band intensity of the bridged hydroxyl group, it was found that the intensity in H-PAR-x (x = 15, 20, 25) sample was higher than that in H-ISO-x sample, even in the case of the same bulk phase composition. Moreover, a shoulder band (3665 cm⁻¹) representing the hydroxyl groups associated with extra framework Al species was obvious in H-ISO-15 sample [44,45]. These results indicated that extra framework Al was present in the H-ISO-x samples, which was most likely due to dealumination. This conclusion is consistent with the results of the ²⁷Al and ²⁹Si spectra in the NMR measurements. As there were many defects in the synthesized crystals, and the framework dealumination occurred during the calcination to remove the SDA, this resulted in fewer [AlO₄]⁻ tetrahedrons in the framework for H-ISO-x samples. Therefore, fewer bridged hydroxyl groups were formed. Regarding samples H-ISO-20 and H-ISO-25, the silanols were the majority of hydroxyl species on their surfaces, whereas the bridged hydroxyls were very small.

It is known that NH₃ adsorption on zeolites leads to the formation of both positive bands (in the range of 3500–3100 cm⁻¹ and 1800–1350 cm⁻¹) and negative bands (3700–3500 cm⁻¹) in the IR spectra, indicating the formation of adsorbed species and consumption of nonacidic/acidic sites [44]. To identify the strength of the acid sites associated with the surface hydroxyl groups, the adsorption spectra were collected after adsorbing NH₃ at 30 °C and 200 °C, and compared with the hydroxyl band of the clean zeolite as the background (Fig. 5a). The results are shown in Fig. 5b and c (details in Figs. S8 and S9, Supplementary material) respectively. When the adsorption is at 30 °C (Fig. 5b), it was determined that almost all hydroxyl species adsorbed ammonia at these low temperatures, resulting in the decay of the

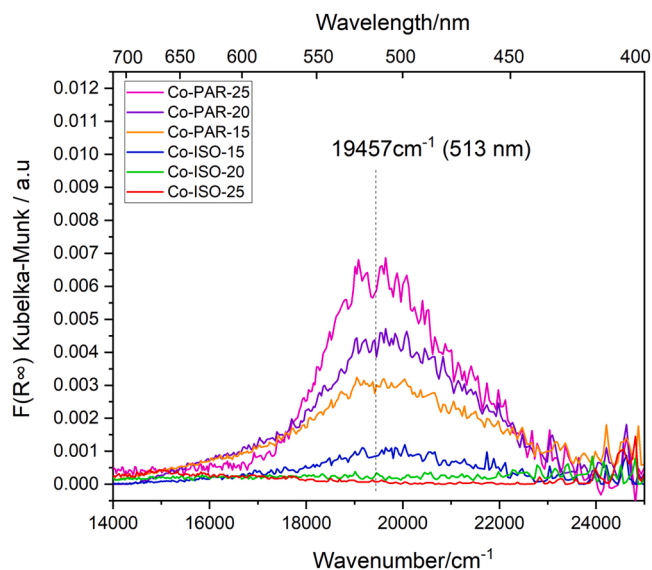


Fig. 4. UV-Vis spectra of rehydrated Co-PAR-x and Co-ISO-x samples (x = 15, 20, 25) at ambient temperature.

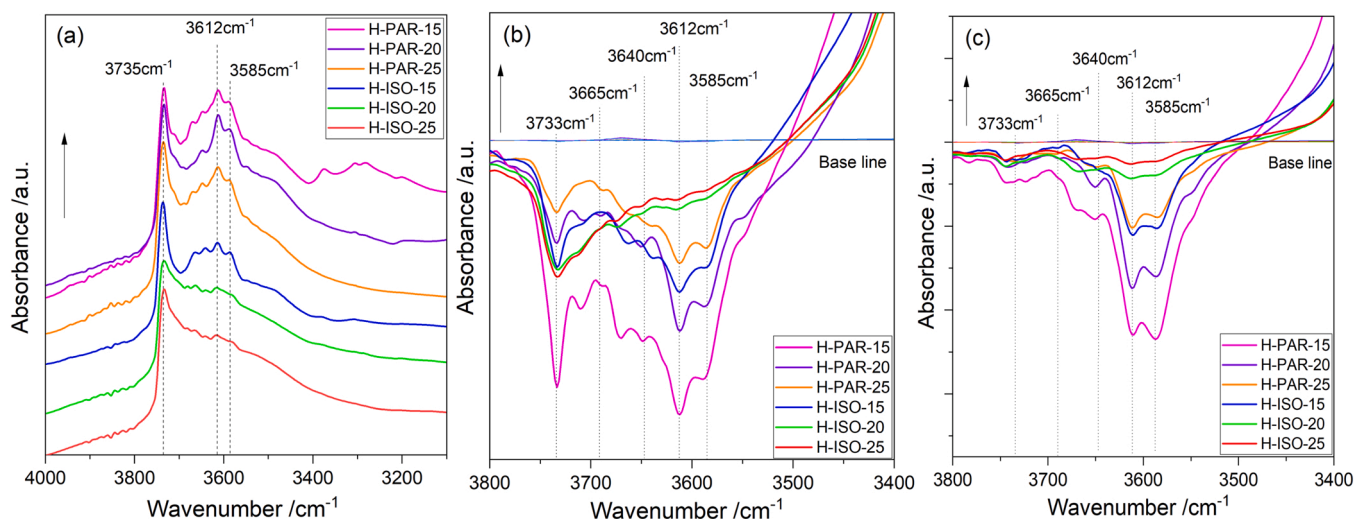


Fig. 5. The IR spectra of hydroxyl groups on the surface of proton-type samples (a), and the corresponding hydroxyl bands after ammonia adsorption at 30 °C (b), or after ammonia adsorption at 200 °C (c).

hydroxyl vibrational band from the reference zero to a negative value. These hydroxyl species included silanols, hydroxyls associated with extra-framework, and bridged hydroxyl species. However, when the adsorption temperature increased to 200 °C (Fig. 5c), the ammonia desorbed from the weak acid sites, and the remaining ammonia only adsorbed on the strong acid sites, which resulted in negative bands at the range of bridged hydroxyl groups (around 3600 cm⁻¹). This result clearly indicated that the acid sites associated with bridged hydroxyl groups are strong acidic sites compared to silanol groups (3733 cm⁻¹) and extra-framework Al hydroxyl groups (3665 cm⁻¹).

There were fewer strong acid sites associated with the bridging hydroxyl groups in the H-ISO-x samples, which further indicates that there were fewer framework Al atoms in its structure. This result is in strong agreement with the NMR experimental results. Although the distribution of aluminum atoms in the framework of H-PAR-x and H-ISO-x samples was different, there was no difference in the produced hydroxyl groups. After the adsorption of ammonia, the vibrational bands of the hydroxyl groups did not undergo any red-shift or blue-shift (see Fig. 5b, c). This means that these acid sites exhibited the same acidic strength towards the adsorbate (ammonia) regardless of the acid site distribution.

Quantification of acid sites of the samples was carried out from the

NH₃-TPD measurements, where the resulting desorption profiles are shown in Fig. 6a and b. In the proton-type samples (Fig. 6a), there were two distinct desorption peaks with peak centers at approximately 200 °C and 500 °C. It can be seen in the above IR results that the desorption peaks at high temperatures were mainly derived from the adsorbed ammonia on the Brønsted acid sites associated with the framework aluminum, and that the peaks at low temperatures were most likely attributed to adsorbed ammonia on nonacidic sites or Lewis acid sites [16]. The intensity of the high-temperature desorption peak increased with the increase of the framework Al content (Fig. 6a), as derived from the NMR measurements in Table 2. Moreover, when the proton-type zeolite was exchanged with sodium cations (Fig. 6b), with the increase of the exchange degree of sodium ions into the zeolite, the intensity of desorption peaks at high temperatures (300–700 °C) gradually decreased, while the peaks at low temperatures (150–300 °C) were gradually broadened. According to the literature, the Brønsted acid sites of zeolites mainly participate in the cation exchange of alkali metal cations. As the exchange proceeded, the Brønsted acid sites are neutralized, and the uptake of alkali metal ions generates new Lewis acid sites [47]. Based on this information, the deconvolution and integration of the desorption peaks, with centers ranging from 300 °C to

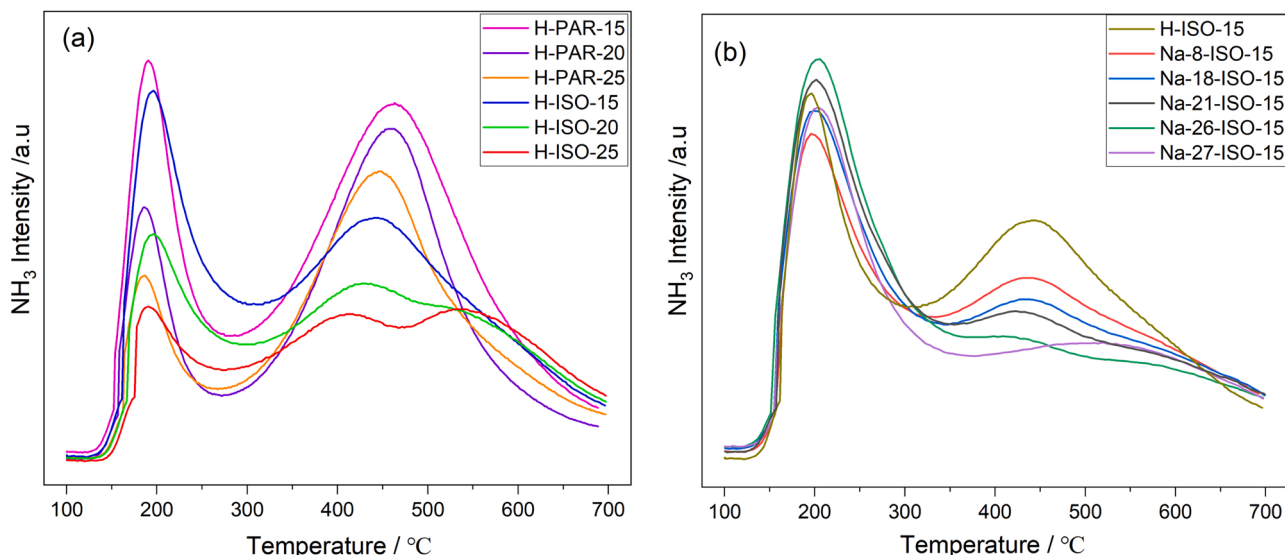


Fig. 6. NH₃-TPD profiles of proton-type zeolite samples (a), and the sodium-type samples prepared by exchanging the H-ISO-15 sample with sodium nitrate (b).

Table 3

Physicochemical properties of sample H-ISO-15 before and after sodium ion exchange.

Sample	Na ^a /wt %	Al ^b /wt %	S _{BET} ^b /m ² *g ⁻¹	V _{micro} ^c /cm ³ *g ⁻¹	Exchange degree ^d /%	BAS density ^e /mmol*g ⁻¹
H-ISO-15	/	2.79	619	0.26	/	0.35
Na-8-ISO-15	0.18	2.73	585	0.25	8%	0.26
Na-18-ISO-15	0.44	2.77	596	0.25	18%	0.23
Na-21-ISO-15	0.51	2.78	570	0.24	21%	0.21
Na-26-ISO-15	0.61	2.73	573	0.24	26%	0.17
Na-27-ISO-15	0.62	2.74	577	0.23	27%	0.15

^a Concentrations of Na and Al elements determined by XRF.

^b BET surface area measured from N₂ adsorption isotherm using BET method.

^c Micropore volume measured from N₂ adsorption isotherm using t-plot method.

^d Exchange degree calculated based on the mole ratio of Na to Al inside the sample after sodium ion exchange.

^e Brønsted acid density assessed from deconvolution of NH₃-TPD curves with centers ranging from 300 °C to 700 °C, details in Fig. S10.

700 °C, were carried out. The results were used to estimate the Brønsted acid site (BAS) density of all zeolite samples, as shown in Tables 2 and 3 (details in Figs. S5, S6 and S10, Supplementary material). It is clear that there is a strong correlation between the amount of BAS density and the ratio of Si/Al in the framework of the samples (Table 2). With the increase of Si/Al in the framework, the BAS density gradually decreased, demonstrating the order of site density according to: H-PAR-15 > H-PAR-20 ≈ H-ISO-15 > H-PAR-25 > H-ISO-20 > H-ISO-25. In Table 3, the sample H-ISO-15 exhibited a strong ability to exchange sodium cations but was unable to take up the cobalt cations due to the isolated acid sites in its framework (Table 1). With the increase of the exchange degree (defined as the ratio of Na/Al mole ratio in the bulk phase), the treated samples exhibited variable BAS density without any change in pore structure or the specific surface area. These can be used as model catalysts to study the effect of Brønsted acid density more exclusively on the catalytic reaction.

3.4. Catalytic performance

Fig. 7 displays the results for CO₂ hydrogenation over the In₂O₃ catalyst, and the bifunctional catalysts as a function of time on stream at 325 °C. The pure In₂O₃ catalysts (M, Fig. 7a) exhibited a stable performance with a CO selectivity of about 90%, and a CO₂ conversion of about 12.3% during 12 h. However, over the bifunctional catalysts consisting of In₂O₃ and zeolite, the CO₂ conversion was increased by approximately 2%, and the CO selectivity significantly decreased by approximately 25–30% with the different zeolite compositions. The promoting effect of bifunctional catalysts has been reported for CO₂ hydrogenation reactions, and it is mainly due to an increased thermodynamic driving force, originating from the rapid conversion of methanol to hydrocarbons over the zeolites [48,49]. Therefore, the conversion of CO₂ to hydrocarbons via the methanol route was facilitated, whereas the reverse water gas shift reaction was inhibited, and the selectivity for CO decreased. In addition, it is worth noting that the methane selectivity was less than 1.2% (among all products) over the pure In₂O₃ catalyst or over the In₂O₃/SSZ-13 bifunctional catalysts (Fig. S12). Unlike for example a ZnCrO_x catalyst, with a methane selectivity up to 53% during CO hydrogenation, which is known to produce ketene. Since there is no zeolite catalyst component to convert the accumulated ketene to olefins, the active ketene intermediate was converted completely to methane [50]. Since the indium oxide catalyst here produced only a small amount of methane, the production route for hydrocarbons predominately follows the methanol intermediate route.

In order to investigate the effect of various SSZ-13 zeolites on the catalytic performance of the bifunctional catalysts, two kinds of proton-type SSZ-13 zeolites were equally mixed with In₂O₃ as bifunctional catalysts and tested. At 325 °C and 10 bar, all SSZ-13 zeolites had a strong MTO reactivity with gradual coke accumulation, however, no deactivation occurred within 12 h (no methanol detected in effluent), given the increased selectivity for light olefins (C₂–C₄) as the reaction proceeded. Compared with the H-PAR-x zeolites (x = 15, 20, 25), the catalysts composed of H-ISO-x zeolites exhibited a higher selectivity for olefins. In particular, the catalyst M/H-ISO-25 with the lowest Brønsted acid site (BAS) density and BET surface areas provided 78% selectivity (based on hydrocarbons) for light olefins after a TOS of 12 h. In contrast, the H-PAR-25 catalyst with the same bulk phase composition gave only 60% selectivity. It is accepted that the MTO reaction, and the hydrogenation reaction can proceed simultaneously on the Brønsted acid sites

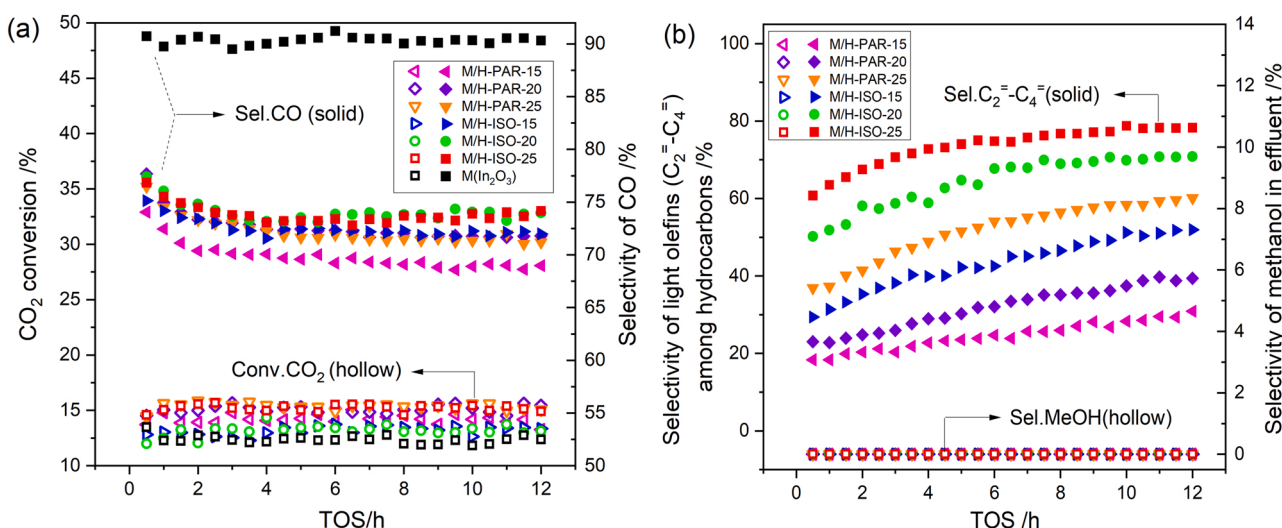


Fig. 7. CO₂ hydrogenation plotted as a function of time on stream (TOS) over In₂O₃ catalysts, or over the bifunctional catalysts of In₂O₃ and SSZ-13. (a) The conversion of CO₂ and selectivity for CO; (b) The selectivity for unconverted methanol and selectivity for light olefins (C₂ to C₄) among hydrocarbons in the effluents. See Fig. S11 (Supplementary material) for additional products. Reaction conditions: Catalyst weight = 1 g, the weight ratio of In₂O₃/SiC = 2 or In₂O₃/SSZ-13 = 2 for pure In₂O₃, or bifunctional catalyst tests respectively, GHSV = 6400 ml*g⁻¹*h⁻¹, T = 325 °C, P = 10 bar, H₂/CO₂ = 6.

of zeolites [15]. It appeared that the zeolite with a higher hydrogenation rate showed higher paraffin selectivity in the early stages of the reaction (Fig. S11). As the reaction progressed, the acid sites were covered by coke deposition, and the pores were modified by coke accumulation, therefore, the hydrogenation rate weakened. Thus, the selectivity for olefins gradually increased as the reaction proceeded. However, the two types of zeolite samples, H-ISO-x and H-PAR-x, have different Brønsted acid densities, Brønsted acid distributions, and porous properties. These different characteristics can all affect the rates of hydrogenation and coke deposition, and therefore it is difficult to determine which factor plays the most decisive role for this catalytic reaction.

In order to further explore the key factors affecting the product distribution, the sample H-ISO-15 was selected as a model zeolite, and its Brønsted acidity was neutralized by sodium cations by ion exchange without changing its porous properties (Table 3). The modified zeolite samples were assembled into bifunctional catalysts and tested. The results in Fig. 8 show that the Brønsted acid site (BAS) density was the key determining factor for product distribution and stability of the catalyst. As the BAS density of the catalyst decreased, both the MTO reaction rate (indicated by higher CO selectivity) and the hydrogenation rate decreased simultaneously, and the catalysts with lower BAS density gave higher selectivity for light olefins. For two catalysts M/H-ISO-20 and M/Na-8-ISO-15 with a similar amount of BAS density (Tables 2 and 3), nearly the same selectivity for light olefins (Fig. 7b and b) was observed. It is worth mentioning that for catalysts M/H-PAR-20 and M/H-ISO-15, although they had almost the same BAS density in their zeolite components, they also showed different performance in their selectivities for light olefins (Fig. 7). This difference may be due to their different Al distributions, but also their different non-framework aluminum content, or different pore structures. It is not possible to distinguish the influence of BAS distribution alone on catalytic performance, because it is inevitably entangled with other varying properties of the SSZ-13 zeolites, since the synthesis methods varying Al distribution also cause different qualities in crystallinity. According to previous conclusions, the H-ISO-15 sample also contained more non-framework aluminum species, and its mesopore volume was larger than that of the H-PAR-20 sample. However, for the sodium ion-exchanged samples, their Al distributions (BAS distribution) were equal, and their pore properties were barely affected. Their BAS density was varied and correlated well with olefin selectivity. Therefore, it is reasonable to conclude that BAS density had the strongest effect on the product distribution.

Reducing the BAS density can improve olefin selectivity, but to a limited extent. When the BAS density of the catalyst was too low, the selectivity for olefins could not be improved. On the contrary, catalyst stability was severely weakened as indicated by methanol beginning to appear in the effluent. During the initial stage of the reaction, it could be seen that the selectivity for CO increased with a decrease in BAS density in the catalysts (Fig. 8a). This was mainly due to the weakened reaction rate of MTO [51], thus, the inhibitory effect on the reverse water gas shift reaction was weakened. Interestingly, when the BAS density of the catalyst decreased to 0.17 mmol·g⁻¹ (for M/Na-26-ISO-15 and M/Na-27-ISO-15 catalysts), the initial period of the MTO reaction was prolonged, resulting in the presence of unreacted methanol in the effluent during the first 1.5 h (Fig. 8b), and an extremely high initial selectivity for CO. As the reaction proceeded, the coke and hydrocarbon pool species gradually accumulated, and the rate of methanol conversion increased, therefore, the unreacted methanol disappeared from the effluent, and the selectivity for CO gradually decreased to a steady-state value. When the reaction continued for 12 h, the active sites of the catalyst became covered or blocked due to the accumulation of coke deposition. The catalysts, therefore, exhibited quick deactivation, which was manifested by the reappearance of unreacted methanol in the effluent and the selectivity for CO increasing slightly again.

3.5. Coking behavior

All spent catalysts were collected and TGA and TPO measurements were carried out in order to analyze the coke deposition on catalysts with different acid densities after TOS of 12 h of the CO₂ reaction. In the TGA curves of Fig. 9a, the weight loss (ΔW_2) which occurred between 300 °C and 700 °C, was used to estimate the coke content inside zeolite during the MTO reaction. Therefore, the TGA patterns for coke in all samples were also normalized based on setting 300 °C as the starting point of 0 wt% in weight loss. It is clear that the BAS density of the zeolite components affected the coke deposition rate in the bifunctional catalyst. When the BAS density of the zeolites was higher than a certain value (approximately 0.25 mmol·g⁻¹), the coke deposition was low, and the amount of coke on the catalysts with different acid densities had few variations. After 12 h of reaction, catalysts M/H-PAR-x and M/H-ISO-x had relatively the same amount of coke deposition (approximately 3 wt%). When the acid density decreased to a lower value (below 0.23 mmol/g), as the BAS density decreased, the amount of coke

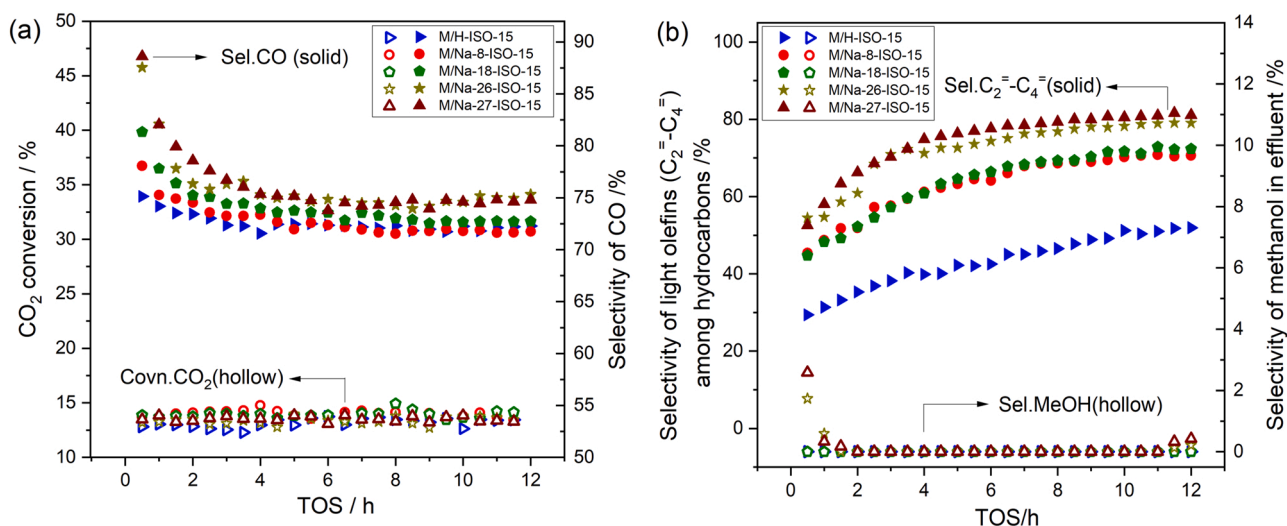


Fig. 8. CO₂ hydrogenation over the bifunctional catalysts of In₂O₃ and SSZ-13 with varying Brønsted acid site densities. (a) The conversion of CO₂ and selectivity for CO; (b) The selectivity for unconverted methanol and light olefins (C₂ to C₄) among hydrocarbons in the effluent. See Fig. S13 (Supplementary material) for additional products. Reaction conditions: Catalyst weight = 1 g, the weight ratio of In₂O₃/SSZ-13 = 2 in granule mixture, GHSV = 6400 ml·g⁻¹·h⁻¹, T = 325 °C, P = 10 bar, H₂/CO₂ = 6.

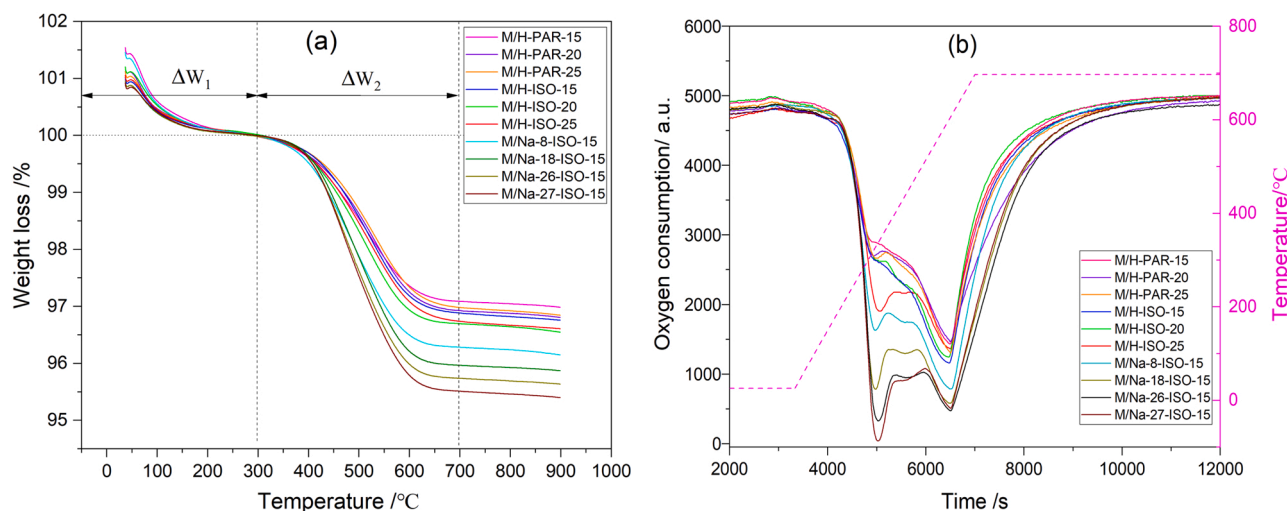


Fig. 9. The TGA patterns (a) and TPO profiles (b) of deposited coke on spent catalysts after CO₂ hydrogenation reaction at temperature of 325 °C, 10 bar, H₂/CO₂ = 6 and after TOS of 12 h.

deposition increased rapidly. For the catalyst samples M/Na-8-ISO-15 to M/Na-27-ISO-15, the amount of coke deposition reached 4.3 wt% for both samples.

The TPO profiles (Fig. 9b) distinguish the resistance to oxidation of the coke associated with the various BAS density of the catalysts. There are two obvious oxidative decomposition peaks, one peak was located at a low temperature centered at approximately 344 °C, and the other is near 600 °C, representing two kinds of coke species. Regarding the catalysts with a BAS density higher than 0.25 mmol·g⁻¹, the low-temperature decomposition peak of coke was not obvious, while the high-temperature decomposition peak dominated, and its area showed little variation with the BAS density. When the BAS density of the catalyst was reduced below 0.23 mmol·g⁻¹, the proportion of the low-temperature peak in their TPO profiles gradually increased, and the decomposition peak area of the whole coke also increased with a decrease in BAS density. The analysis of the soluble coke in the spent catalysts by GC-MS further confirmed that the composition of coke was closely associated with the BAS density (Figure S14, Supplementary material). On catalysts with high BAS density, the deposited coke were light methylbenzenes, mainly including toluene to tetra-methylbenzene. When the BAS density gradually decreased, in addition to light methylbenzene, the penta-methylbenzene, hexa-methylbenzene, and adamantane species appeared in larger quantities on the spent catalysts (Fig. S14). It is well known that methylbenzenes are generally considered to be hydrocarbon pool species (HCPs), which catalyze the MTO reaction together with Brønsted acid centers while adamantane species are generally considered the main species that cause the rapid MTO deactivation at low temperatures (300–400 °C) [13,52]. Therefore, there is reason to speculate that too low BAS density leads to deactivation of the catalyst, possibly due to the large amount of inactive adamantane species. A more detailed characterization and identification of the relevant hydrocarbon pool and coking species on the same catalysts have been discussed in another paper from our group [53]. Regarding the catalyst M/Na-27-ISO-15 with the lowest BAS density, the largest amount of adamantane deposition on its surface further confirmed its rapid inactivation performance during reaction (Fig. 8b). This also demonstrates that the BAS density of catalysts should not be too low, but instead in some optimal range for best performance. The catalysts with too low BAS density showed fast adamantane deposition rates, leading to quick catalyst deactivation without increasing the selectivity for olefins further.

In Fig. 10, the effect of the BAS density on the selectivity for CO, the selectivity for light olefins among hydrocarbons, and the selectivity for

unreacted methanol in the initial period (0.5 h), as well as the coke deposition after 12 h TOS were summarized for the CO₂ hydrogenation experiments. Among these all the catalysts with varying Al distributions and porous properties, it can be clearly seen that the BAS density exhibits a good correlation with the selectivity for light olefins and coke deposition in CO₂ hydrogenation. This demonstrates that the BAS density of the zeolite component in the bifunctional catalysts is the decisive factor for olefin production. It can also be seen that the BAS density of the optimal catalyst needed to be within a reasonable range to maintain both a high selectivity for olefins and stability of the catalyst. The ideal BAS density in the zeolite component was approximately 0.25 mmol/g for these experimental conditions. The zeolite with this value was the H-ISO-20 sample, which was synthesized using TMA⁺ as the sole SDA. It exhibited a strained Brønsted acidity after calcination in order to remove the SDA, however, it was a good zeolite component in the bifunctional catalysts for the hydrogenation of CO₂ to light olefins. After 12 h reaction at 325 °C and 10 bar, it gave 70% selectivity for light olefins among hydrocarbons, and 74% selectivity for CO without deactivation.

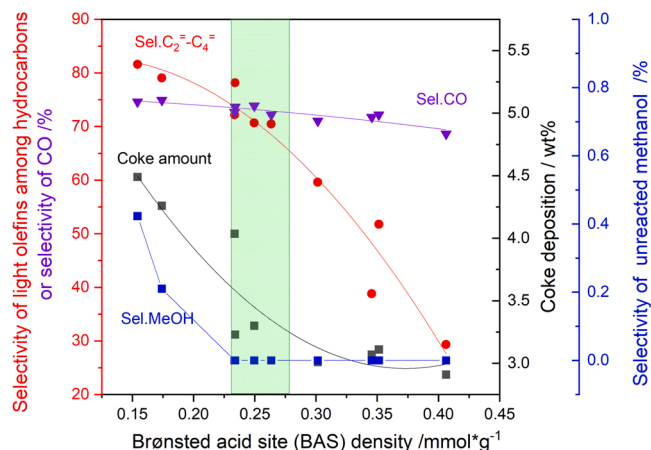


Fig. 10. Effect of the Brønsted acid site (BAS) density of zeolite component on the catalytic performance of the bifunctional In₂O₃/SSZ-13 catalysts. (1) the selectivity for light olefins (C₂–C₄), (2) coke deposition amount, (3) the selectivity for unreacted methanol at TOS of 0.5 h. Reaction condition: Catalyst weight = 1 g, the weight ratio of In₂O₃/SSZ-13 = 2 in granule mixture, GHSV = 6400 ml·g⁻¹·h⁻¹, T = 325 °C, P = 10 bar, H₂/CO₂ = 6. TOS = 12 h.

4. Conclusions

In the range of Si/Al molar ratios from 15–30, SSZ-13 zeolites with only isolated Al distribution in the framework have been successfully synthesized using TMAda⁺ as the sole SDA. However, due to the lack of small cations in the SDA composition during the crystallization, this synthesized zeolite had many defects in its structure. A higher Si/Al in the bulk phase, caused more defect sites in the framework. After high-temperature calcination, the zeolite with defect sites underwent framework dealumination, showing lower crystallinity and lower specific surface area. However, the crystal morphology was maintained. Compared with the SSZ-13 zeolites containing paired Al, which were synthesized using the conventional mixture of Na⁺ cations and TMAda⁺ as the SDA, the zeolites with isolated Al distribution preserved less framework aluminum. As a result, the isolated Al distribution zeolites exhibited lower content of bridged hydroxyl groups and lower Brønsted acid site (BAS) densities. However, there was no difference in their Brønsted acid strength, regardless of different Al distributions. When combining these zeolites and indium oxides as bifunctional catalysts, these lower acidic zeolites with isolated Al distribution, demonstrated better reactivity compared with those containing paired Al distribution during low temperature CO₂ hydrogenation. Comparative experiments using Na⁺ cation exchange to adjust the BAS density in the zeolite with isolated Al distribution, further showed that the BAS density rather than BAS distribution of the zeolite was the decisive factor affecting the product distribution and catalyst stability in CO₂ hydrogenation. With too high BAS density, the rates of the MTO and hydrogenation reactions were rapid, giving a lower selectivity for CO due to the thermodynamic driving force effect. Paraffins were the main hydrocarbon products, and the rate of coke accumulation was low. With too low BAS density, the rates of the MTO and hydrogenation reactions were slowed down, giving a longer initial period for the MTO reaction, and a weak effect on decreasing the selectivity for CO. Light olefins were the main hydrocarbon products, but the inert adamantanes in coke quickly accumulated, and thus the catalyst deactivated rapidly. An ideal catalyst was found to have a BAS density of around 0.25 mmol/g, which exhibited 70% selectivity for light olefins among hydrocarbons and 74% selectivity for CO without deactivation, after 12 h time-on-stream at 325 °C and 10 bar.

CCRediT authorship contribution statement

Wei Di: Conceptualization, Writing – original draft, Writing – review & editing, Investigation, Methodology, Validation, Data curation, Visualization. **Phuoc Hoang Ho:** Investigation, Methodology. **Abdenour Achour:** Investigation, Methodology. **Oleg Pajalic:** Supervision, Writing – review & editing. **Lars Josefsson:** Supervision, Writing – review & editing. **Louise Olsson:** Conceptualization, Writing – review & editing, Funding acquisition, Project administration, Supervision. **Derek Creaser:** Conceptualization, Writing – review & editing, Funding acquisition, Supervision.

Declaration of Competing Interest

The authors declare the following financial interests/personal relationships which may be considered as potential competing interests: Louise Olsson reports financial support was provided by Swedish Energy Agency. Oleg Pajalic reports a relationship with Perstorp Specialty Chemicals AB that includes: employment. co-author: Lars Josefsson, employed by his own company Josefsson Sustainable Chemistry AB.

Data availability

Data will be made available on request.

Acknowledgments

This project was conducted at the Chemical Engineering Division, the Competence Centre for Catalysis (KCK) and the Centre for Process Chemical Engineering (CPE) at Chalmers University of Technology, and was performed in collaboration with Perstorp AB and Josefsson Sustainable Chemistry AB. We gratefully acknowledge the funding from Swedish Energy Agency (P49617–1). Special acknowledgments should be addressed to the Swedish NMR Centre node at Umeå University for support.

Appendix A. Supporting information

Supplementary data associated with this article can be found in the online version at doi:10.1016/j.jcou.2023.102512.

References

- [1] E. Ra, K. Kim, E. Kim, H. Lee, K. An, J. Lee, Recycling carbon dioxide through catalytic hydrogenation: recent key developments and perspectives, *ACS Catal.* 10 (2020) 11318–11345.
- [2] G.A. Olah, G.K.S. Prakash, A. Goepfert, Anthropogenic chemical carbon cycle for a sustainable future, *J. Am. Chem. Soc.* 133 (2011) 12881–12898.
- [3] B. Pawelec, R. Guil-López, N. Mota, J.L.G. Fierro, R.M.N. Yerga, Catalysts for the conversion of CO₂ to low molecular weight olefins—a review, *Materials* 14 (2021) 6952.
- [4] P. Gao, S. Dang, S. Li, X. Bu, Z. Liu, M. Qiu, C. Yang, H. Wang, L. Zhong, Y. Han, Q. Liu, W. Wei, Y. Sun, Direct production of lower olefins from CO₂ conversion via bifunctional catalysis, *ACS Catal.* 8 (2018) 571–578.
- [5] Z. Li, J. Wang, Y. Qu, H. Liu, C. Tang, S. Miao, Z. Feng, H. An, C. Li, Highly selective conversion of carbon dioxide to lower olefins, *ACS Catal.* 7 (2017) 8544–8548.
- [6] X. Liu, M. Wang, C. Zhou, W. Zhou, K. Cheng, J. Kang, Q. Zhang, W. Deng, Y. Wang, Selective transformation of carbon dioxide into lower olefins with a bifunctional catalyst composed of ZnGa₂O₄ and SAPO-34, *Chem. Commun.* 54 (2018) 140–143.
- [7] R. Ye, J. Ding, W. Gong, M.D. Argyle, Q. Zhong, Y. Wang, C.K. Russell, Z. Xu, A. G. Russell, Q. Li, M. Fan, Y.G. Yao, CO₂ Hydrogenation to High-Value Products via Heterogeneous Catalysis, *Nat. Commun.* 10 (2019) 5698.
- [8] O. Martín, A.J. Martín, C. Mondelli, S. Mitchell, T.F. Segawa, R. Hauert, C. Drouilly, D. Curulla-Ferré, J. Pérez-Ramírez, Indium Oxide as a Superior Catalyst for Methanol Synthesis by CO₂ Hydrogenation, *Angew. Chem., Int. Ed.* 55 (2016) 6261–6265.
- [9] M.S. Frei, C. Mondelli, A. Cesarini, F. Krumeich, R. Hauert, J.A. Stewart, D. Curulla Ferré, J. Pérez-Ramírez, Role of Zirconia in Indium Oxide-Catalyzed CO₂ Hydrogenation to Methanol, *ACS Catal.* 10 (2019) 1133–1145.
- [10] J. Wang, G. Li, Z. Li, C. Tang, Z. Feng, H. An, H. Liu, T. Liu, C. Li, A highly selective and stable ZnO–ZrO₂ solid solution catalyst for CO₂ hydrogenation to methanol, *Sci. Adv.* 3 (10) (2017), e1701290.
- [11] N. Ortner, D. Zhao, H. Mena, J. Wei, H. Lund, S. Bartling, S. Wohlrab, U. Armbruster, E.V. Kondratenko, Revealing Origins of Methanol Selectivity Loss in CO₂ Hydrogenation over CuZn-Containing Catalysts, *ACS Catal.* 13 (2023) 60–71.
- [12] J. Chen, X. Wang, D. Wu, J. Zhang, Q. Ma, X. Gao, X. Lai, H. Xia, S. Fan, T.S. Zhao, Hydrogenation of CO₂ to light olefins on CuZnZr@ (Zn-) SAPO-34 catalysts: Strategy for product distribution, *Fuel* 239 (2019) 44–52.
- [13] P. Tian, Y. Wei, M. Ye, Z. Liu, Methanol to Olefins (MTO): from fundamentals to commercialization, *ACS Catal.* 5 (2015) 1922–1938.
- [14] D.L.S. Nieskens, J.D. Lunn, A. Malek, Understanding the enhanced lifetime of SAPO-34 in a direct syngas-to-hydrocarbons process, *ACS Catal.* 9 (2019) 691–700.
- [15] M. DeLuca, C. Janes, D. Hibbitts, Contrasting Arene, Alkene, Diene, and Formaldehyde Hydrogenation in H-ZSM-5, H-SSZ-13, and H-SAPO-34 Frameworks during MTO, *ACS Catal.* 10 (2020) 4593–4607.
- [16] S.S. Arora, D.L.S. Nieskens, A. Malek, et al., Lifetime improvement in methanol-to-olefins catalysis over chabazite materials by high-pressure H₂ co-feeds, *Nat. Catal.* 1 (2018) 666–672.
- [17] X. Zhao, J. Li, P. Tian, L. Wang, X. Li, S. Lin, X. Guo, Z. Liu, Achieving a Superlong Lifetime in the Zeolite-Catalyzed MTO Reaction under High Pressure: Synergistic Effect of Hydrogen and Water, *ACS Catal.* 9 (2019) 3017–3025.
- [18] K. Leistner, L. Olsson, Deactivation of Cu/SAPO-34 during low-temperature NH₃-SCR, *Appl. Catal. B: Environ.* 165 (2015) 192–199.
- [19] M.A. Deimund, L. Harrison, J.D. Lunn, Y. Liu, A. Malek, R. Shayib, M.E. Davis, Effect of Heteroatom Concentration in SSZ-13 on the Methanol-to-Olefins Reaction, *ACS Catal.* 6 (2016) 542–550.
- [20] Z. Li, J. Martínez-Triguero, J. Yu, A. Corma, Conversion of methanol to olefins: Stabilization of nanosized SAPO-34 by hydrothermal treatment, *J. Catal.* 329 (2015) 379.
- [21] F. Bleken, M. Bjørgen, L. Palumbo, S. Bordiga, S. Svelle, K.P. Lillerud, U. Olsbye, The effect of acid strength on the conversion of methanol to olefins over acidic microporous catalysts with the CHA topology, *Top. Catal.* 52 (2009) 218–228.
- [22] Z. Shi, M. Neurock, A. Bhan, Methanol-to-Olefins Catalysis on HSSZ-13 and HSAPO-34 and Its Relationship to Acid Strength, *ACS Catal.* 11 (2021) 1222–1232.

- [23] Z. Liu, Y. Ni, T. Sun, W. Zhu, Z. Liu, Conversion of CO₂ and H₂ into propane over InZrOx and SSZ-13 composite catalyst, *J. Energy Chem.* 54 (2021) 111–117.
- [24] S. Lu, H. Yang, C. Yang, P. Gao, Y. Sun, Highly selective synthesis of LPG from CO₂ hydrogenation over In₂O₃/SSZ-13 bifunctional catalyst, *J. Fuel Chem. Technol.* 49 (8) (2021) 1132–1139.
- [25] Z. Liu, Y. Ni, M. Gao, L. Wang, X. Fang, J. Liu, Z. Chen, N. Wang, P. Tian, W. Zhu, Z. Liu, Simultaneously achieving high conversion and selectivity in syngas-to-propane reaction via a dual-bed catalyst system, *ACS Catal.* 12 (2022) 3985–3994.
- [26] Y. Huang, H. Ma, Z. Xu, W. Qian, H. Zhang, W. Ying, Direct conversion of syngas to light olefins over a ZnCrOx+H-SSZ-13 Bifunctional Catalyst, *ACS Omega* 6 (2021) 10953–10962.
- [27] M. Dusselier, M.A. Deimund, J.E. Schmidt, M.E. Davis, Methanol-to-olefins catalysis with hydrothermally treated zeolite SSZ-39, *ACS Catal.* 5 (2015) 6078–6085.
- [28] H. Zhang, Q. Li, Y. Mou, L. Bing, F. Wang, D. Han, G. Wang, Tuning product selectivity in the MTO reaction over Zn-modified SSZ-13 catalysts, *N. J. Chem.* 46 (2022) 19046–19053.
- [29] T. Nishitoba, N. Yoshida, J.N. Kondo, T. Yokoi, Control of Al distribution in the CHA-type aluminosilicate zeolites and its impact on the hydrothermal stability and catalytic properties, *Ind. Eng. Chem. Res.* 57 (2018) 3914–3922.
- [30] J.R. Di Iorio, C.T. Nimlos, R. Gounder, Introducing catalytic diversity into single-site chabazite zeolites of fixed composition via synthetic control of active site proximity, *ACS Catal.* 7 (2017) 6663–6674.
- [31] J.R. Di Iorio, R. Gounder, Controlling the isolation and pairing of aluminum in chabazite zeolites using mixtures of organic and inorganic structure-directing agents, *Chem. Mater.* 28 (2016) 2236–2247.
- [32] X. Liu, M. Wang, H. Yin, J. Hu, K. Cheng, J. Kang, Q. Zhang, Y. Wang, Tandem catalysis for hydrogenation of CO and CO₂ to lower olefins with bifunctional catalysts composed of spinel oxide and SAPO-34, *ACS Catal.* 10 (2020) 8303–8314.
- [33] A. Hwang, M. Kumar, J. Rimer, A. Bhan, Implications of methanol disproportionation on catalyst lifetime for methanol-to-olefins conversion by HSSZ-13, *J. Catal.* 346 (2017) 154–160.
- [34] S. Ghosh, J. Sebastian, L. Olsson, D. Creaser, Experimental and kinetic modeling studies of methanol synthesis from CO₂ hydrogenation using In₂O₃ catalyst, *Chem. Eng. J.* 416 (2021), 129120.
- [35] S. Lee, C.T. Nimlos, E.R. Kipp, Y. Wang, X. Gao, W.F. Schneider, M. Lusardi, V. Vattipalli, S. Prasad, A. Moini, R. Gounder, Evolution of Framework Al Arrangements in CHA Zeolites during Crystallization in the Presence of Organic and Inorganic Structure-Directing Agents, *Cryst. Growth Des.* 22 (2022) 6275–6295.
- [36] J. Dědeček, D. Kaucký, B. Wichterlová, O. Gonsiorová, Co²⁺ ions as probes of Al distribution in the framework of zeolites. ZSM-5 study, *Phys. Chem. Chem. Phys.* 4 (2002) 5406–5413.
- [37] T. Usui, Z. Liu, S. Ibe, J. Zhu, C. Anand, H. Igarashi, N. Onaya, Y. Sasaki, Y. Shiramata, T. Kusamoto, T. Wakihara, Improve the hydrothermal stability of Cu-SSZ-13 zeolite catalyst by loading a small amount of Ce, *Acs. Catal.* 8 (2018) 9165–9173.
- [38] Database of Zeolite Structures, <http://www.iza-structure.org/databases/> (accessed December 20, 2022)
- [39] M. Kumar, H. Luo, Y. Román-Leshkov, J.D. Rimer, SSZ-13 crystallization by particle attachment and deterministic pathways to crystal size control, *J. Am. Chem. Soc.* 137 (2015) 13007–13017.
- [40] Z. Xu, H. Ma, Y. Huang, W. Qian, H. Zhang, W. Ying, Synthesis of Submicron SSZ-13 with tunable acidity by the seed-assisted method and its performance and coking behavior in the MTO reaction, *ACS Omega* 5 (2020) 24574–24583.
- [41] K. Mlekodaj, J. Dedeczek, V. Pashkova, E. Tabor, P. Klein, M. Urbanova, R. Karcz, P. Sazama, S.R. Whittleton, H.M. Thomas, A.V. Fishchuk, Al organization in the SSZ-13 zeolite. Al distribution and extraframework sites of divalent cations, *J. Phys. Chem. C* 123 (2019) 7968–7987.
- [42] C. Jia, P. Massiani, D. Barthomeuf, Characterization by infrared and nuclear magnetic resonance spectroscopies of calcined beta zeolite, *J. Chem. Soc. FARADAY TRANS* 89 (1993) 3659–3665.
- [43] M.W. Borer, S.R. Maple, Control of spinning sidebands in high resolution NMR spectroscopy, *J. Magn. Reson.* 131 (1998) 177–183.
- [44] S.A. Skarlis, D. Berthout, A. Nicolle, C. Dujardin, P. Granger, I.R. Spectroscopy, Analysis and Kinetic Modeling Study for NH₃ Adsorption and Desorption on H- and Fe-BEA Catalysts, *J. Phys. Chem. C* 117 (2013) 7154–7169.
- [45] S. Bordiga, L. Regli, D. Cocina, C. Lamberti, M. Bjørgen, K.P. Lillerud, Assessing the Acidity of High Silica Chabazite H - SSZ-13 by FTIR Using CO as Molecular Probe: Comparison with H-SAPO-34, *J. Phys. Chem. B* 109 (2005) 2779–2784.
- [46] M. Ravi, V.L. Sushkevich, J.A. van Bokhoven, On the location of Lewis acidic aluminum in zeolite mordenite and the role of framework-associated aluminum in mediating the switch between Brønsted and Lewis acidity, *Chem. Sci.* 12 (2021) 4094–4103.
- [47] Y. Ji, H. Yang, W. Yan, Effect of alkali metal cations modification on the acid/basic properties and catalytic activity of ZSM-5 in cracking of supercritical n-dodecane, *Fuel* 243 (2019) 155–161.
- [48] X. Liu, W. Zhou, Y. Yang, K. Cheng, J. Kang, L. Zhang, G. Zhang, X. Min, Q. Zhang, Y. Wang, Design of efficient bifunctional catalysts for direct conversion of syngas into lower olefins via methanol/dimethyl ether intermediates, *Chem. Sci.* 9 (2018) 4708–4718.
- [49] S. Ghosh, L. Olsson, D. Creaser, Methanol mediated direct CO₂ hydrogenation to hydrocarbons: Experimental and kinetic modeling study, *Chem. Eng. J.* 435 (2022), 135090.
- [50] F. Jiao, J. Li, X. Pan, J. Xiao, H. Li, H. Ma, M. Wei, Y. Pan, Z. Zhou, M. Li, S. Miao, Selective conversion of syngas to light olefins, *Science* 351 (2016) 1065–1068.
- [51] E. Borodina, F. Meirer, I. Lezcano-González, M. Mokhtar, A.M. Asiri, S.A. Al-Thabaiti, S.N. Basahel, J. Ruiz-Martinez, B.M. Weckhuysen, Influence of the reaction temperature on the nature of the active and deactivating species during methanol to olefins conversion over H-SSZ-13, *Acs. Catal.* 5 (2015) 992–1003.
- [52] Y. Wei, J. Li, C. Yuan, S. Xu, Y. Zhou, J. Chen, Q. Wang, Q. Zhang, Z. Liu, Generation of diamondoid hydrocarbons as confined compounds in SAPO-34 catalyst in the conversion of methanol, *Chem. Commun.* 48 (2012) 3082–3084.
- [53] W. Di, A. Achour, P.H. Ho, S. Ghosh, O. Pajalic, L. Josefsson, L. Olsson, D. Creaser, Modulating the formation of coke to improve the production of light olefins from CO₂ hydrogenation over In₂O₃ & SSZ-13 catalysts. (Submitted to Journal of CO₂ Utilization, Manuscript number: JCOU-D-23-00149).